An Investigation of the Goshen County, Wyoming, Tornadic Supercell of 5 June 2009 Using EnKF Assimilation of Mobile Mesonet and Radar Observations Collected during VORTEX2. Part I: Experiment Design and Verification of the EnKF Analyses

JAMES MARQUIS, YVETTE RICHARDSON, AND PAUL MARKOWSKI

Department of Meteorology, The Pennsylvania State University, University Park, Pennsylvania

DAVID DOWELL

NOAA/Earth System Research Laboratory, Boulder, Colorado

JOSHUA WURMAN, KAREN KOSIBA, AND PAUL ROBINSON

Center for Severe Weather Research, Boulder, Colorado

GLEN ROMINE

National Center for Atmospheric Research, Boulder, Colorado

(Manuscript received 31 December 2012, in final form 25 September 2013)

ABSTRACT

High-resolution Doppler radar velocities and in situ surface observations collected in a tornadic supercell on 5 June 2009 during the second Verification of the Origins of Rotation in Tornadoes Experiment (VORTEX2) are assimilated into a simulated convective storm using an ensemble Kalman filter (EnKF). A series of EnKF experiments using a 1-km horizontal model grid spacing demonstrates the sensitivity of the cold pool and kinematic structure of the storm to the assimilation of these observations and to different model microphysics parameterizations. An experiment is performed using a finer grid spacing (500 m) and the most optimal data assimilation and model configurations from the sensitivity tests to produce a realistically evolving storm. Analyses from this experiment are verified against dual-Doppler and in situ observations and are evaluated for their potential to confidently evaluate mesocyclone-scale processes in the storm using trajectory analysis and calculations of Lagrangian vorticity budgets. In Part II of this study, these analyses will be further evaluated to learn the roles that mesocyclone-scale processes play in tornado formation, maintenance, and decay. The coldness of the simulated low-level outflow is generally insensitive to the choice of certain microphysical parameterizations, likely owing to the vast quantity of kinematic and in situ thermodynamic observations assimilated. The three-dimensional EnKF wind fields and parcel trajectories resemble those retrieved from dual-Doppler observations within the storm, suggesting that realistic four-dimensional mesocyclone-scale processes are captured. However, potential errors are found in trajectories and Lagrangian three-dimensional vorticity budget calculations performed within the mesocyclone that may be due to the coarse (2 min) temporal resolution of the analyses. Therefore, caution must be exercised when interpreting trajectories in this area of the storm.

1. Introduction

The Goshen County, Wyoming, supercell of 5 June 2009 (hereafter, the Goshen County storm), targeted by the second Verification of the Origins of Rotation in Tornadoes Experiment (VORTEX2; Wurman et al. 2012), is likely the most thoroughly observed tornadic supercell in history. The Doppler on Wheels radars (DOWs; Wurman et al. 1997), the National Severe Storms Laboratory's (NSSL) mobile X-band dual-polarimetric radar (NOXP; Palmer et al. 2009), mobile mesonets (Straka et al. 1996; Waugh and Fredrickson 2010), the Texas Tech Sticknet (Weiss and Schroeder

Corresponding author address: James N. Marquis, The Pennsylvania State University, 503 Walker Bldg., University Park, PA 16802.
E-mail: jmarquis@met.psu.edu

DOI: 10.1175/MWR-D-13-00007.1

2008), and other instruments collected wind data throughout the storm and thermodynamic data near the ground during the intercept. These observations have exposed several of the finescale processes believed to have played roles in the generation, maintenance, and decay of low-level vorticity (Markowski et al. 2012a,b; Kosiba et al. 2012; Richardson et al. 2012).

Despite the large quantity of data collected in this case, the relatively small size of the dual-Doppler lobes [typical coverage area is ~20 km × 20 km × 4 km assuming a 30° minimum interbeam angle; see Fig. 4 in Markowski et al. (2012a) for a radar deployment map of the intercept] and general lack of velocity observations outside of precipitating regions of the storm preclude a more complete understanding of how the low-level mesocyclone and tornado interact with distant features of the storm. For example, we cannot confidently comment on the deep vertical structure of the mesocyclone, updrafts, and downdrafts, which may be important for the diagnosis of processes relating to tornado behavior (e.g., Markowski 2002; Dowell and Bluestein 2002; Marquis et al. 2012). Knowledge of the origins of air entering the mesocyclone during certain periods of the tornado life cycle is obscured owing to the curtailed length of trajectories when they reach the edges of the dual-Doppler coverage. Furthermore, errors in the trajectory calculations are introduced by the need to extrapolate velocity data below the radar horizon in the dual-Doppler syntheses (located 100–300 m above ground level in this case). Mobile mesonet in situ observations were collected only at 2 m above the ground, with horizontal coverage dictated by the network of passable roads. Therefore, the regions of the storm containing substantial baroclinity, which may modulate the horizontal vorticity that is tilted into the vertical along-parcel trajectories entering the near-surface mesocyclone (e.g., Rotunno and Klemp 1985; Davies-Jones and Brooks 1993; Wicker and Wilhelmson 1995), and possibly substantial negative buoyancy, which may inhibit the contraction of low-level angular momentum toward the axis of rotation (e.g., Markowski et al. 2003), are sometimes inadequately sampled near the ground and are completely unsampled above it. Thermodynamic analyses spanning a wider area and depth are needed to gain a thorough understanding of the mesocyclone-scale processes influencing tornado formation and maintenance.

Over the last decade, various studies have demonstrated the utility of assimilating radar observations into a numerical simulation of a convective storm in a cloud-resolving model using the ensemble Kalman filter technique (EnKF) as a tool for initializing the model for a future forecast or for the evaluation of storm dynamics at assimilation time steps. Snyder and Zhang (2003) first demonstrated the potential accuracy of EnKF retrievals of unobserved kinematic and thermodynamic fields by assimilating synthetic single-Doppler radar velocities drawn from a control simulation of a supercell storm. Subsequent studies, such as those of Zhang et al. (2004), Dowell et al. (2004), Aksoy et al. (2009), Dowell and Wicker (2009), Dowell et al. (2011), Jung et al. (2012), Tanamachi et al. (2012), Yussouf and Stensrud (2012), and Dawson et al. (2012), tested the sensitivity of the results from similar EnKF experiments (either assimilating real observations or simulated observations taken from a control model solution) to methods of ensemble initialization, methods to maintain ensemble spread, the quality of the assimilated observations, the assimilation of radar reflectivity or in situ observations, the choice of model microphysics, and the representation of the mesoscale environment. Using recommendations from some of these studies, Marquis et al. (2012) assimilated single-Doppler radar velocities collected in tornadic supercells into simulations of convective storms in order to expand the amount of four-dimensional data available for a multicase comparison of storm- and mesocyclone-scale processes relating to tornado maintenance. Their EnKF analyses enabled the evaluation of outflow buoyancy and tornado placement relative to the midlevel updraft, both of which were considered important aspects of tornado maintenance not directly observed in their storms.

In this study, we follow a similar methodology to that employed by Marquis et al. (2012) to produce ensemble-mean EnKF kinematic and thermodynamic analyses and use them to enhance the observational dataset of the Goshen County storm. There are a few notable differences between the Goshen County dataset and those used in Marquis et al., including the VORTEX2 collection of surface in situ observations and a much larger quantity of nearly simultaneous mobile radar observations across several radar platforms. We assimilate the near-surface temperature and moisture observations to assist in obtaining realistic cold pools used in the evaluation of low-level baroclinity and vorticity generation in the storm. Furthermore, we test the sensitivity of the model results to the inclusion of different microphysics parameters, which have been shown to directly impact the behavior of simulated outflow, low-level updraft, downdraft, and vorticity structures (e.g., Gilmore et al. 2004; Dawson et al. 2010; Morrison and Milbrandt 2011). In this first part of our two-part study, we justify the design of our high-resolution (500-m horizontal grid spacing) EnKF assimilation experiments using the results from a series of coarser-resolution (1-km grid spacing) experiments designed to optimize the assimilation of the radar and in situ observations (sections 2

and 3). We verify the resulting high-resolution kinematic and thermodynamic analyses with the available dual-Doppler wind syntheses and surface mobile mesonet observations and compare EnKF Lagrangian three-dimensional vorticity budget terms integrated along parcel trajectories to the EnKF ensemble-mean vorticity analyses (section 4). A near match in these Lagrangian budgets should indicate a realistic temporal evolution of our EnKF analyses, garnering even greater confidence in their utility for the investigation of the storm. Our findings are summarized in section 5. In a forthcoming paper (J. Marquis et al., unpublished manuscript, hereafter Part II), we will use the EnKF analyses to diagnose the influence of mesocyclone-scale processes on tornado behavior in the Goshen County supercell.

2. Method

We refer the reader to Snyder and Zhang (2003) for a detailed introduction to EnKF assimilation of radar data in a convective-scale model. Our simulations use the nonhydrostatic Advanced Research core of the Weather Research and Forecasting Model (WRF v3.2.1; Skamarock et al. 2008). We use a horizontal grid spacing of 500 m (1000 m in our sensitivity tests) and prescribe mass levels corresponding to a stretched vertical coordinate with a spacing of approximately 80 m near the ground and 2 km at the top of the domain. The domain dimensions are 135 km $\times$ 80 km $\times$ 20 km. We use 1.5-order turbulence closure, open lateral boundary conditions with an assumed gravity wave speed of 25 m s^{-1}, a Rayleigh damping layer in the uppermost 5 km of the domain to prevent wave reflection off the domain ceiling, and sixth-order numerical diffusion (reduction factor of 0.12) to reduce the $2\Delta x$ noise. We use the single-moment Lin et al. (1983, hereafter LFO) ice microphysics parameterization with graupel and rain intercept parameters of 4 and 8×10^6 m^{-4}, respectively, and a graupel density of 900 kg m^{-3} (as in Gilmore et al. 2004). (Other microphysics schemes are tested in section 3.) The model time step is 2 s and the experiment duration is approximately 2 h. Convective updrafts are initiated 10 min prior to the start of data assimilation by placing 10 ellipsoidal warm bubbles within a 30 km $\times$ 30 km $\times$ 2 km box that contains high (>20 dBZ) radar reflectivity observations. The bubbles have a maximum potential temperature (θ) perturbation of 4 K, and a radius of 10 (1.5) km in the horizontal (vertical) direction. The placement of each warm bubble within the box is random for each ensemble member.

Our idealized modeling strategy, owing to computational constraints, assumes flat terrain. The actual average (westward pointing) zonal elevation gradient in the geographic region corresponding to the model domain is about (600 m)/(150 km), and the elevation drop along the path of the tornado is approximately 100 m (roughly one vertical grid interval in the lowest part of the model domain). Surface fluxes and radiative transfer are absent from the simulations. The horizontally homogeneous initial model state is derived from a VORTEX2 rawinsonde that was launched in the inflow area of the supercell approximately 50 km south-southeast of the storm near the time of tornadogenesis (2155 UTC). The surface temperature and vapor mixing ratio r_v are modified to be consistent with the average mobile mesonet observations in the near-storm inflow, and the sounding subsequently is adjusted so that the θ and r_v profiles are linear from the surface to the base of the capping inversion. The modified and raw soundings are shown in Fig. 1.

a. Observations assimilated

Doppler radial velocities from four radars [DOW6, DOW7, NOXP, and the Cheyenne, Wyoming (KCYS), Weather Surveillance-1988 Doppler (WSR-88D)], as well as mobile mesonet θ and specific humidity (q_v) observations, are assimilated at 2-min intervals (Fig. 2). The elevation angle list for each radar volume assimilated includes 0.5°–16° (DOWs), 0.5°–11° (NOXP), and 0.5°–19.5° (KCYS), with six and eight sweeps below 5.0° for the mobile radars and KCYS, respectively. Radar sweeps are individually objectively analyzed onto a grid with a regular horizontal Cartesian spacing equal to that of the model horizontal grid spacing but with radar beam heights specified along the original conical surfaces at each grid point (Sun and Crook 2001; Dowell et al. 2004). Objective analysis is performed using a Cressman weighting with a radius of influence equal to the horizontal grid spacing. Objectively analyzed radial velocities are assumed to have an error variance of (2 m s^{-1})^2 (Dowell et al. 2004). The mobile mesonet in situ observations were collected at a frequency of 1 hz, are smoothed with a 10-s triangular temporal filter, and contain assumed error variances of (1 K)^2 and (1 g kg^{-1})^2 for θ and q_v observations, respectively. They are assimilated at the lowest model grid level.

To spin up the modeled storms before high-resolution radar data were collected, the first DOW7 radar volume (collected from 2130 to 2131 UTC) is repeatedly assimilated at 2-min intervals during the 2045–2130 UTC period using an average storm motion and a steady-state assumption in the storm reference frame (cf. Marquis et al. 2012). We assimilate the DOW7 volume under these assumptions rather than assimilating the KCYS observations actually collected during this period because of the higher resolution and lower radar beam horizon of

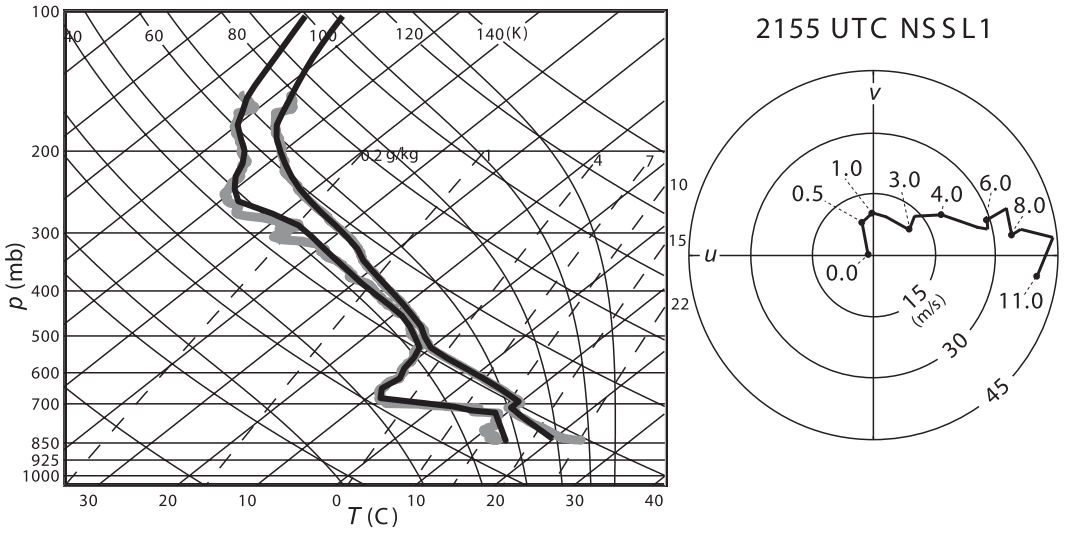

FIG. 1. Skew T–log$p$ diagram and hodograph of the 2155 UTC 5 Jun 2009 NSSL 1 sounding used to define the horizontally homogeneous model environment. The gray thermodynamic profile is the raw sounding. The black profile is the modified form used in the model. The heights AGL (km) of several points on the hodograph are shown.

DOW7 (the distance between DOW7 and the hook echo is approximately 33 km versus 60 km for KCYS at 2131 UTC; the corresponding radar horizons in the hook echo are z = 250 and 600 m for DOW7 and KCYS, respectively). The resulting storm develops more realistic low-level updraft, downdraft, and cold pool structure when the DOW7 2130 UTC radar volume is repeatedly assimilated than when KCYS observations are assimilated. During this period of repeated assimilation, we assume the same radar velocity error variance as for the actual observations. Although it is at least partly countered by our use of additive noise and adaptive inflation, it is possible that this assumption could yield an overfit of the ensemble to the observations (Annan et al. 2005). No conclusions are drawn from the EnKF analyses prior to 2131 UTC owing to this possibility and the assumption of steadiness that accompanies the repeated assimilation of a single DOW7 radar volume.

b. Specific EnKF implementation

Observations are assimilated into WRF using the Data Assimilation Research Testbed software (DART; Anderson et al. 2009). We use the ensemble adjustment filter method (Anderson 2001) to control the effects of an underestimated analysis-error covariance associated with using an ensemble of a finite size. The model u, v, w, and θ and the mixing ratios of water vapor, rain, graupel, cloud water, snow, and ice are updated at each assimilation step. Our ensemble comprises 50 members. Our localization is a correlation function from Gaspari and Cohn (1999), equal to 1.0 at the location of an observation and decreasing to a value of 0.0 at a distance of 6 km for radar observations and 18 km for mobile mesonet observations. Ensemble spread is maintained throughout the data assimilation experiments using two methods. First, by adding random Gaussian noise to the model u, v, θ, and r_v[1] fields at 2-min intervals in locations having a logarithmic radar reflectivity factor of at least 25 dBZ (Dowell and Wicker 2009). The perturbation fields are smoothed to spatial scales of 4 km in the horizontal and 2 km in the vertical and have standard deviations of 0.1 K (for θ and T_d) and 0.2 m s^{-1} (for u and v). The magnitudes of these perturbations are kept smaller than most tested in Dowell and Wicker, because larger values sometimes produced unrealistic warm or cold anomalies that remained in the ensemble-mean analyses for several assimilation cycles, even when added to the model fields less frequently (4- and 6-min intervals). Second, we use an adaptive inflation technique (Anderson 2009) to augment the ensemble spread. The volume-mean root-mean-square innovation (rmsi) and total spread [a metric including both ensemble spread and observation error; see Eqs. (3.2) and (3.3) in Dowell and Wicker 2009] for the radar and mobile mesonet observations shown in Fig. 3. Several variations of these two mechanisms for maintaining ensemble spread were tested. It was difficult to find a combination that provides adequate spread and that did not produce noisy thermodynamic analyses. Typically, the total spread was larger than the rmsi, with

[1] Perturbations actually are added to T_d rather than r_v to prevent possibly generating negative values of r_v. Dewpoint temperature is then converted back to r_v.

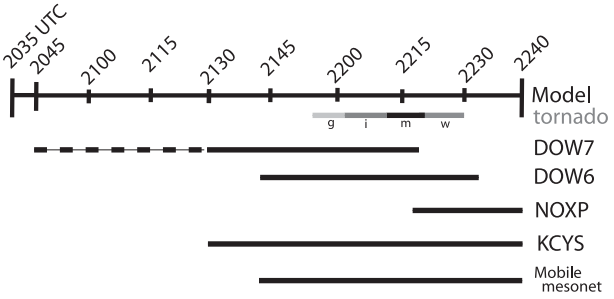

FIG. 2. Times (UTC) corresponding to the model duration and the assimilation windows of the radar velocity observations and mobile mesonet thermodynamic observations. The dashed line indicates the ensemble spinup period when the 2130 UTC DOW7 radar volume is repeatedly assimilated. The approximate periods of tornadogenesis, intensification, maturity, and weakening also are shown (labeled g, i, m, and w, respectively).

ensemble spread (excluding observation error) often relatively small, suggesting a general underfit of the observations, particularly for the mobile mesonets. Our final experiment is the one in which the forecast rmsi is the lowest.

3. Coarse-resolution sensitivity tests

While deciding upon the methodology outlined above, we performed a series of EnKF experiments that explored the sensitivity of the analyses to certain model and data assimilation parameterizations. For computational ease, each of these experiments is performed using a horizontal model grid spacing that is coarser than in our final experiments (1 versus 0.5 km). However, at this grid resolution, updraft, downdraft, vorticity, and outflow structures are qualitatively similar to experiments on a 500-m grid, suggesting applicability of the sensitivity findings to our finest grid spacing.

Approximately 9 million objectively analyzed radar observations on a 500-m grid are available for assimilation. Motivated by the computational cost incurred by our 500-m grid experiments, we tested the sensitivity of the kinematic analyses to the density of the radar observations assimilated. We conducted three experiments that are identical in design except for the number of assimilated radar radial velocity observations that are objectively analyzed onto a 1-km horizontal grid; one experiment assimilates all objectively analyzed observations, while two others assimilate 50% and 25% of the observations (observation density is evenly distributed on the x and y grids in both experiments). A fourth experiment also tests the sensitivity of the EnKF analyses to different resolved scales in the observations by assimilating all that are objectively analyzed onto a 2-km horizontal grid (again, using a 1-km model grid spacing).

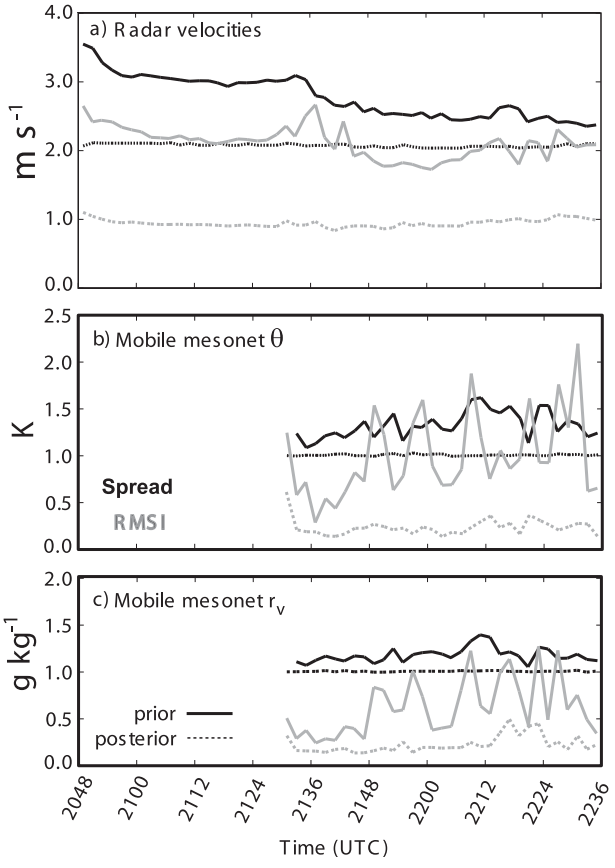

FIG. 3. The rmsi (gray lines) and total spread (a combination of observation error and ensemble spread; black lines) for (a) radial velocities from all radars, (b) θ, and (c) r_v from the mobile mesonets in 2-min time bins calculated using posterior (dotted lines) and prior (solid lines) analyses. Quantities are as described in Dowell and Wicker (2009).

The low-level kinematic structure produced in these four experiments is compared to dual-Doppler wind syntheses produced using a 1-km horizontal grid spacing and a Cressman weighting in Fig. 4. In general, low-level vertical vorticity and horizontal convergence fields along the gust fronts and within downdrafts on the forward and rear flanks of the storm are insensitive to thinning of the 1-km observations by 50% (Figs. 4b,c), and compare qualitatively well to the structure produced in the dual-Doppler syntheses (Figs. 4a). Though convergence along the gust front and the basic spatial structures of the vertical vorticity maximum and divergence in the downdrafts are preserved when only 25% of the 1-km observations are assimilated (Fig. 4d), the magnitudes of the divergence and vertical vorticity are slightly weakened and do not verify against the dual-Doppler syntheses quite as well. Assimilated 2-km grid observations yield smoother and weaker divergence and vertical vorticity along the rear flank of the storm

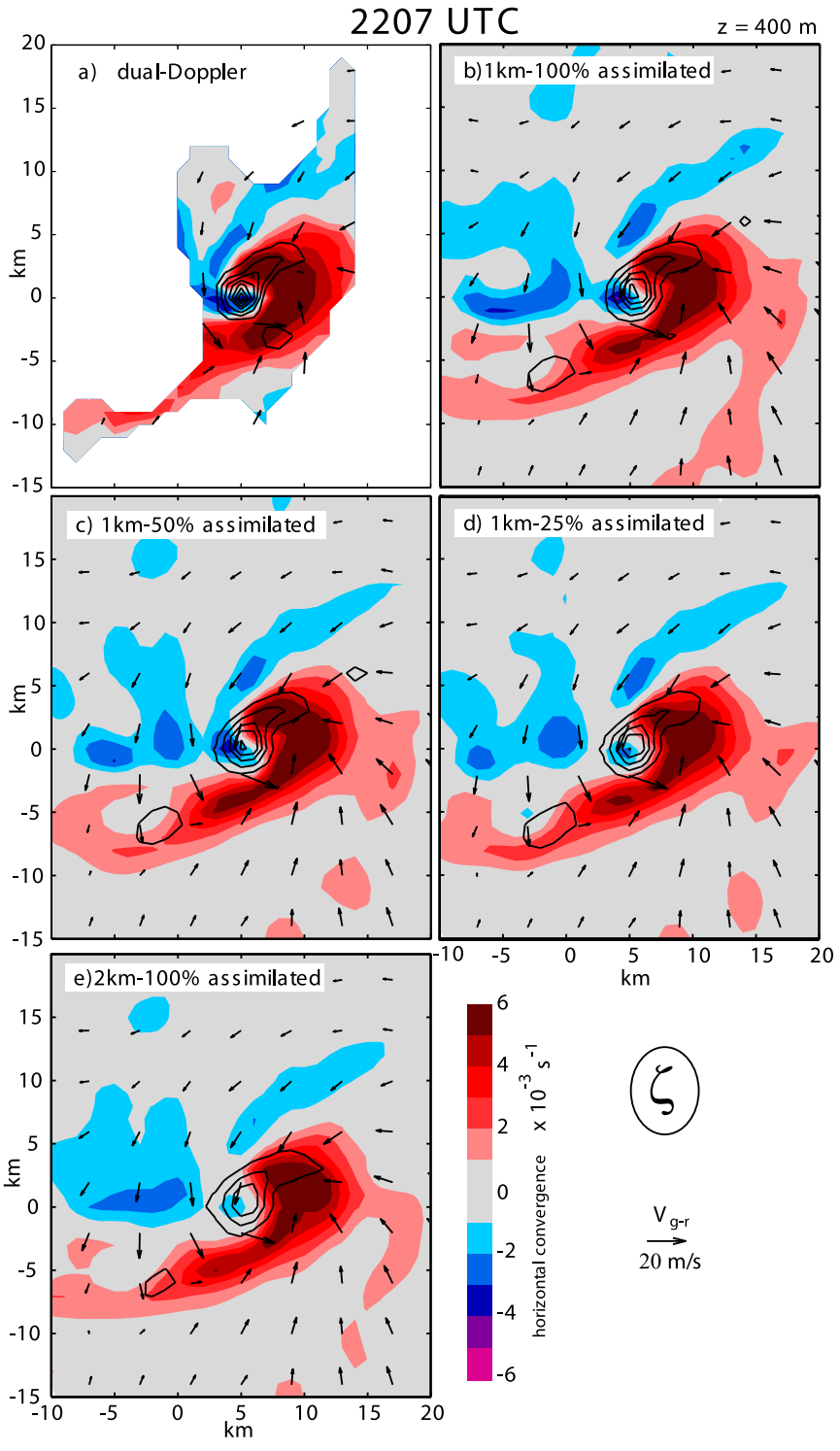

FIG. 4. Horizontal convergence (shaded), vertical vorticity (solid black contours, outermost is 0.0025 s^{-1}, incremented by 0.005 s^{-1}), and ground-relative wind vectors at $z = 400$ m AGL at 2207 UTC. (a) Dual-Doppler syntheses of these kinematic fields. (b)–(e) Posterior ensemble-mean analyses of these fields from four data assimilation experiments performed on a model grid with a 1-km horizontal spacing. These experiments are identical except for the density or resolution of observations assimilated: (b) all observations objectively analyzed onto a 1-km horizontal grid are assimilated, (c) 50% of the observations on a 1-km grid are assimilated, (d) 25% of the observations on a 1-km grid are assimilated, and (e) all observations objectively analyzed onto a 2-km horizontal grid are assimilated.

(Fig. 4e). Based on these experiments, we elected to assimilate 50% of the observations objectively analyzed onto a horizontal grid spacing that matches the model. These results are not intended to determine an optimal ratio between the resolved scales of the model and observations. Such optimality may be better assessed when using a more controlled dataset, as within an observing system simulation experiment (OSSE) framework.

Properties of the outflow have been demonstrated in numerous studies to have a great impact on mesocyclone and tornado formation, maintenance, and decay. Furthermore, several modeling studies have demonstrated the sensitivity of outflow characteristics using different model microphysics schemes. To ensure that we produce the most accurate cold pool possible, we performed a series of experiments to test the sensitivity of our analyses to the choice of model microphysics schemes available in WRF v3.2.1. Six experiments in which only radar velocities are assimilated are identical except for the microphysics schemes. Four use the LFO single-moment ice microphysics scheme but vary the rain and graupel intercept parameters; one uses rain and graupel intercept parameters of $8 \times 10^6\,\mathrm{m}^{-4}$ and $4 \times 10^4\,\mathrm{m}^{-4}$, respectively, with a graupel density of $900\,\mathrm{kg\,m}^3$ (e.g., those tested in Gilmore et al. 2004), while the remaining three match those parameters with the following exceptions: (i) a graupel intercept parameter of $4 \times 10^3\,\mathrm{m}^{-4}$, (ii) a rain intercept parameter of $8 \times 10^5\,\mathrm{m}^{-4}$, and (iii) a rain intercept parameter of $1 \times 10^7\,\mathrm{m}^{-4}$. These variations span a range of values that other investigators have tested in past research (e.g., L. Wicker 2013, personal communication). Two other experiments use the Milbrandt and Yau (2005a,b) and the Morrison et al. (2005) dual-moment schemes. Examples of the low-level kinematic and temperature structure when each of these schemes is used are shown in Fig. 5. The LFO experiments yield generally cooler outflow temperatures than do the dual-moment experiments, consistent with simulations from Dawson et al. (2010), and also exhibit overall smaller differences between the ensemble-mean potential temperature at the lowest model scalar grid level and the mobile mesonet surface observations than the dual-moment schemes (especially the Milbrandt–Yau scheme).

There is little sensitivity of the kinematic fields to the choice of model microphysics, presumably owing to the large quantity of radar velocities assimilated. The areas of the cold pool that most differ among the schemes and often verify the most poorly using mobile mesonet observations are located >5 km northwest through southwest of the mesocyclone where relatively few velocity observations were collected in the clear air. The LFO schemes differ by smaller amounts elsewhere in the cold pool, where a greater density of radar observations exists. Outflow near the mesocyclone tends to be slightly colder or the forward-flank outflow is slightly warmer when the average rain and graupel size is increased (Figs. 5a–d). Smaller raindrops tend to make the forward-flank outflow slightly cooler than when larger rain drops are used (Figs. 5a,c,d). Each of these trends is perhaps consistent with differing horizontal advection of hydrometeors downstream of the updraft based on their relative sizes. However, in general, differences in cold pool temperature among the LFO schemes are less than 1–3 K throughout the well-observed portion of the storm, and none of the tested LFO schemes verified against the available in situ observations better than the one using the Gilmore et al. (2004) intercept parameter set. We were unable to further isolate the effects of using these microphysics schemes on the outflow in the Goshen County environment in the absence of data assimilation because free forecasts of this storm in idealized simulations (i.e., without data assimilation) failed to result in realistically evolving storms using several variations of the sounding in Fig. 1.

To increase the accuracy of the simulated cold pool, we assimilated the in situ thermodynamic observations collected in the storm by the mobile mesonet vehicles. We are unaware of past attempts to assimilate such a large quantity of in situ surface observations capable of resolving mesocyclone-scale features into a modeled supercell. Therefore, to determine how to optimize their influence on the ensemble, we tested the sensitivity of the EnKF analyses to the assimilation of the mobile mesonet observations using different vertical and horizontal localization distances and different microphysics schemes. Early attempts to assimilate these in situ observations employed a localization that decreased to zero at a horizontal distance of 6 km (same as for the radar velocities). Such experiments produced cold pools that contained thermodynamic anomalies along the paths traversed by the mobile mesonets, but did not spread information contained in the observations to model grid locations far from the actual road network (not shown). A localization that decreases to zero at a horizontal distance of 18 km seemed to adequately extend the radius of influence through unobserved portions of the model domain within the storm. Figure 6 compares near-surface ensemble-mean θ and r_v analyses in the outflow from an experiment that assimilates radar and mobile mesonet observations to one in which only radar observations are assimilated. In general, the assimilation of mobile mesonet θ and q_v chilled and moistened the near-surface outflow temperature, decreasing the overall difference between observed and EnKF θ and r_v from as high as 4.5 K and $2.5\,\mathrm{g\,kg}^{-1}$,

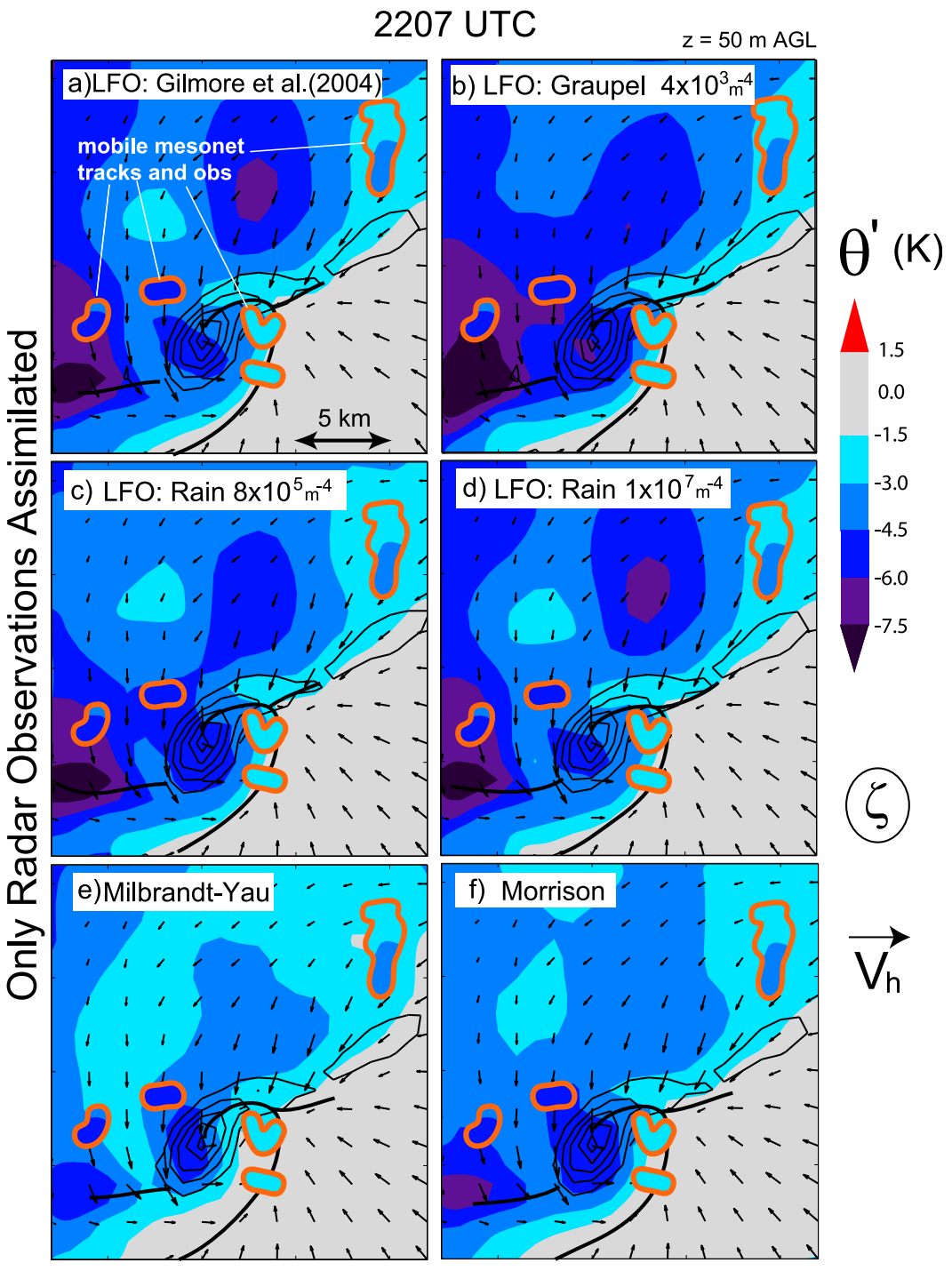

FIG. 5. Posterior ensemble-mean potential temperature deficit (θ', shaded), vertical vorticity (black contours; outermost contour is $0.003\,s^{-1}$, incremented by $0.005\,s^{-1}$), and ground-relative horizontal velocity (vectors) at the lowest model scalar grid level ($z = 50$ m) at 2207 UTC from six data assimilation experiments, each using a different microphysics parameterization: (a) the LFO scheme with rain and graupel intercept parameters of $8 \times 10^6\,m^{-4}$ and $4 \times 10^4\,m^{-4}$, respectively; (b) as in (a), but using a graupel intercept parameter of $4 \times 10^3\,m^{-4}$; (c) as in (a), but using a rain intercept parameter of $8 \times 10^5\,m^{-4}$; (d) as in (a), but using a rain intercept parameter of $1 \times 10^7\,m^{-4}$; (e) using the Milbrandt and Yau (2005a,b) dual-moment scheme; and (f) using the Morrison et al. (2005) dual-moment scheme. Traces of the updraft maximum along the gust fronts are traced in thick black lines. Time-to-space-converted mobile mesonet tracks using an average storm motion valid within 1 min of 2207 UTC are overlain on the ensemble-mean fields (orange swaths). The color fill within each orange swath represents the in situ observations of θ' collected by each mesonet using the same color scale as the gridded ensemble-mean θ' field.

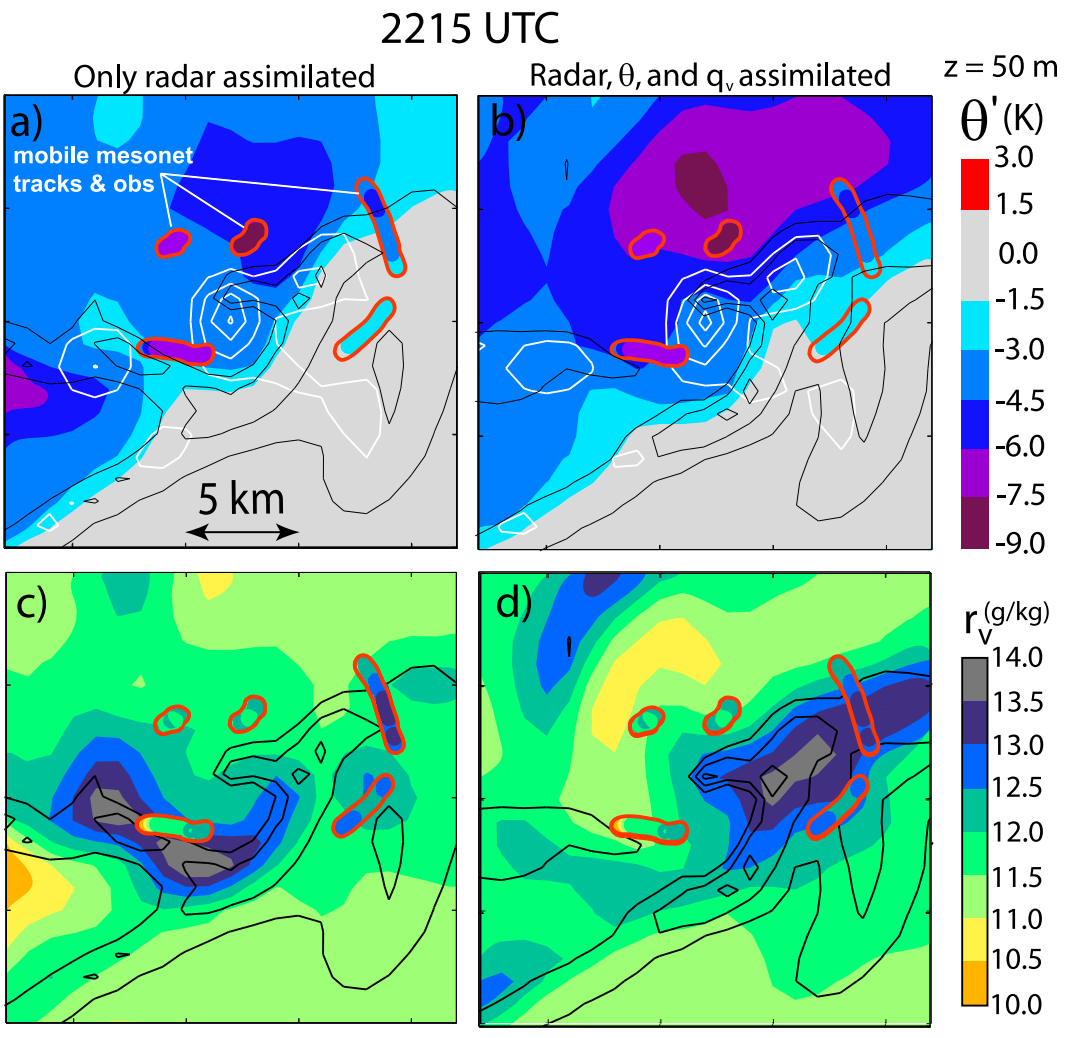

FIG. 6. (a),(b) Posterior ensemble-mean θ' (shaded), vertical vorticity (white contours; outermost contour is $0.005\,s^{-1}$, incremented by $0.01\,s^{-1}$), and updraft (black contours; outermost contour is $0.25\,m\,s^{-1}$, incremented by $0.25\,m\,s^{-1}$) at the lowest model scalar grid level ($z = 50\,m$) from two experiments that are identical except for the types of observations assimilated: (left) only radar velocities are assimilated and (right) radar and mobile mesonet θ and q_v observations are assimilated. (c),(d) As in (a),(b), but for ensemble-mean r_v. Ensemble-mean vertical vorticity is omitted for clarity. Time-to-space-converted mobile mesonet observations of θ' and r_v valid within 1 min of the EnKF analysis time are overlain (orange swaths with observations color filled).

respectively, to 3 K and $1\,g\,kg^{-1}$ (Fig. 7). The greatest changes in outflow temperature occurred in the forward-flank baroclinic zone and on the left flank of the storm near the precipitation core at low levels (Figs. 6a,b). The assimilation of q_v generally moistened the simulated storm the most in the forward-flank baroclinic region (Figs. 6c,d). The assimilated surface θ and q_v observations within the outflow impact the storm most in the lowest 2–3 km, indicating that they influence little above the cold pool even when the localization zero point is at a height of 18 km (Fig. 8).

Assimilating these observations affects other aspects of the storm possibly related to outflow production comparatively subtly (Fig. 9). Peak updraft strength below $z = 3$ km is generally insensitive to the assimilation of surface observations. Updraft strength aloft is slightly more sensitive when employing a deep vertical localization cutoff, but the profile of $|w|$ is qualitatively similar and different by $\leq 2\,m\,s^{-1}$ (Fig. 9a). The strength of the downdraft near the mesocyclone (i.e., the rear-flank downdraft at low and midlevels) is slightly more sensitive to the assimilation of the surface observations throughout low levels than the updraft, but differences are generally $\leq 1.5\,m\,s^{-1}$. Furthermore, the surface observations impact the peak downdraft aloft even with a shallow vertical localization cutoff, suggesting an

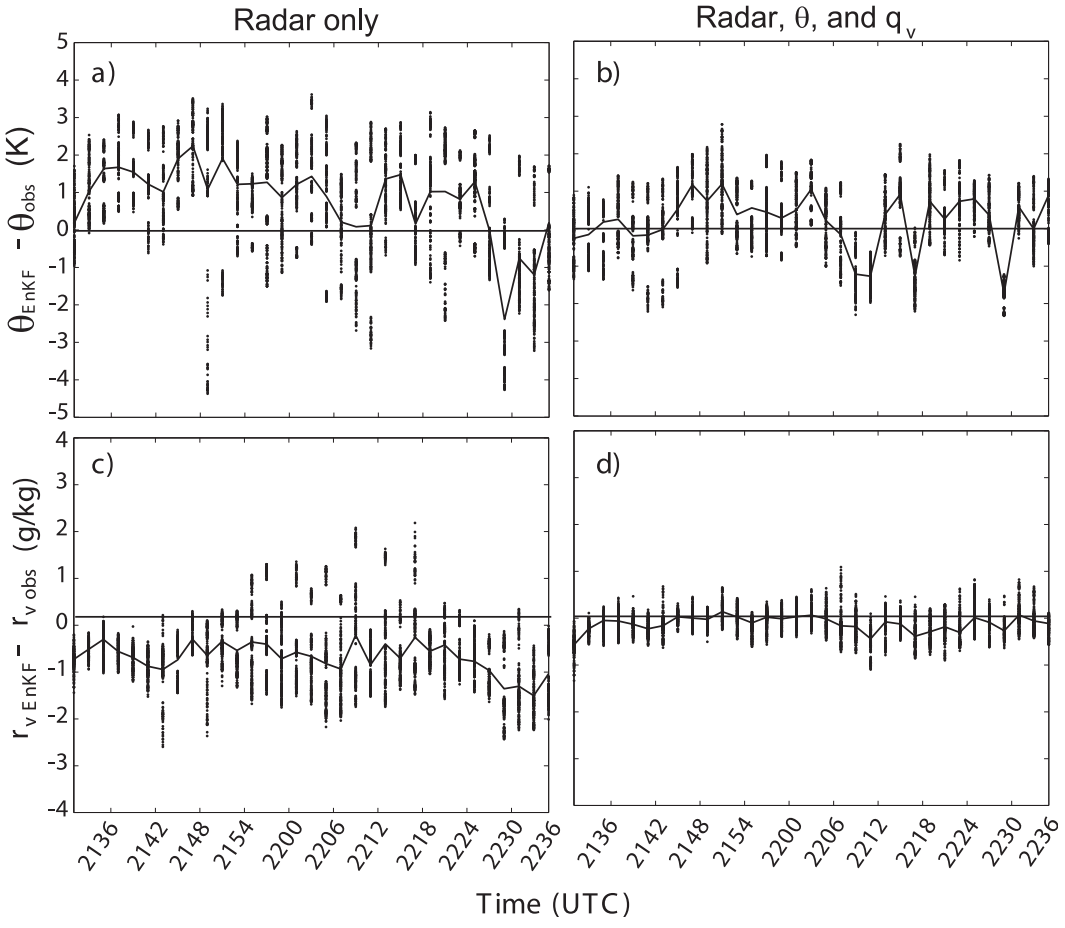

FIG. 7. Differences between mobile mesonet observations of (a),(b) θ and (c),(d) r_v, and ensemble-mean analyses interpolated to the positions of the mobile mesonets as a function of time, calculated from an experiment assimilating (left) only radar velocities and (right) radar velocities and mobile mesonet θ and q_v. The difference between each observation and the ensemble-mean value at that location is shown as one dot at each EnKF analysis time. The average of these differences at each time is traced with a solid line.

indirect impact by the surface observations via integration of the model equations between assimilation cycles[2] (Fig. 9b). The effects of assimilating q_v have an obvious impact on r_v in the outflow, but these observations have a very small impact on the midlevel environment and result in r_v differences of up to 1.0 g kg^{-1} in the lowest 3 km (Fig. 9d). Similar qualitative changes are seen in the ensemble-mean rain mixing ratio fields (r_{rain}) (Fig. 9c). A deep vertical localization cutoff does not seem to alter the r_v or r_{rain} analyses significantly more than does a shallower one. Without knowing the true state of the storm, it is unclear whether assimilating surface observations in the cold pool produces more accurate results aloft. However, noting the overall small differences in most fields aloft, we set 6 km as the vertical distance at which the localization decreases to zero.

The differences in the cold pool characteristics among the six microphysics experiments are decreased when the surface observations also are assimilated (cf. Figs. 5 and 10). Forward-flank baroclinicity and the buoyancy within the low-level mesocyclone vary only subtly among all six of the microphysics experiments. Differences in ensemble-mean θ' are generally less than 1.5 K, and the forecast spread in the ensemble is decreased and virtually identical, regardless of single- or dual-moment microphysics parameterizations (Fig. 11). These results suggest *the assimilation of a large density of radar velocity and surface observations may help to offset the uncertainty in*

[2] The profiles in Fig. 9 are from experiments that assimilate mobile mesonet observations in the outflow for approximately 30 min (about 15 assimilation cycles) prior to the time shown. When surface observations are assimilated only at the analysis time shown (one assimilation cycle), differences among the three experiments are comparatively small and the impact of differing vertical localization cutoffs are more apparent.

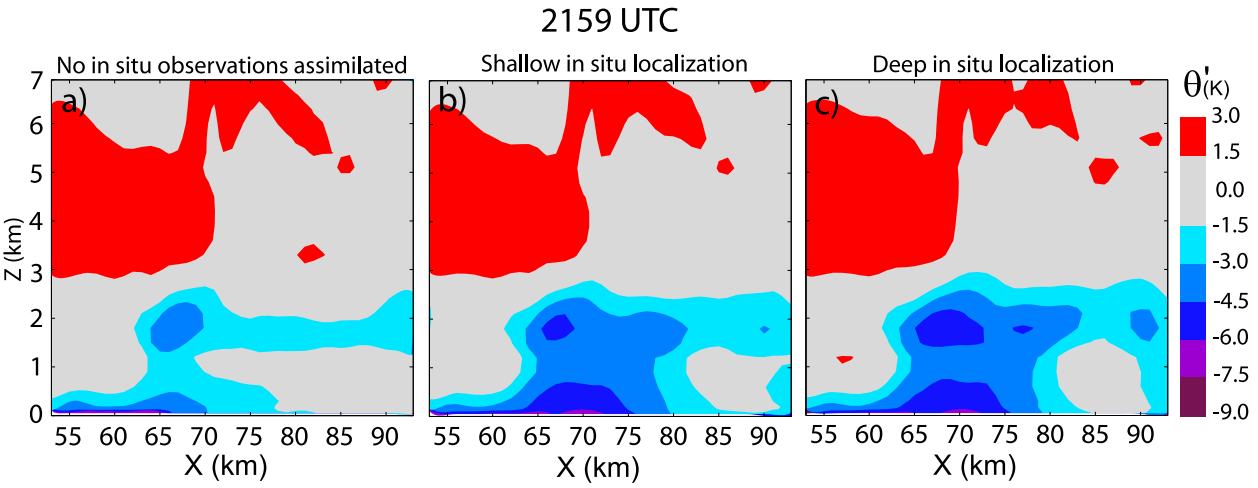

FIG. 8. Ensemble-mean θ' from the environment along an east–west vertical cross section slicing through the forward-flank cold pool and tracks of two mobile mesonets on the ground at 2159 UTC. Cross sections are from three experiments that are identical except that (a) no mobile mesonet observations are assimilated (only radar velocities), (b) mobile mesonet θ and q_v observations are assimilated with a vertical localization that reduces to zero at 6 km, and (c) as in (b), but the vertical localization reduces to zero at 18 km. Horizontal localizations for all mobile mesonet observations reduce to zero at 18 km.

the analyses generated by some model parameterizations, such as microphysics schemes, permitting a greater confidence in the retrieved storm structure. However, it is not clear if this result can be generalized for other cases and should be pursued in future work.

4. Verification of high-resolution analyses

a. Kinematic analyses

Based on our relatively coarse-resolution (1-km grid spacing) sensitivity tests, our final experiment is performed using the criteria described in sections 2 and 3 with a finer model grid resolution (500-m grid spacing). Figures 12 and 13 compare a sequence of EnKF ensemble-mean analyses of select low-level kinematic fields from this 500-m-grid experiment to dual-Doppler wind syntheses. To facilitate the dual-Doppler synthesis, DOW6 and DOW7 velocities are objectively analyzed onto a Cartesian grid with a 500-m (200 m) horizontal (vertical) grid spacing using a Cressman scheme with a radius of influence of 800 m. The dual-Doppler three-dimensional wind fields are then produced by iteratively integrating the anelastic mass continuity equation upward from the ground (e.g., Brandes 1977; Ray et al. 1980). Artificial tilt of the storm due to its motion during the radar volume collection period is prevented by adjusting the horizontal positions of the velocity data to the central time of the radar volume using an average storm motion vector. To apply the lower boundary condition for the upward integration ($w = 0$ at $z = 0$), a profile of constant horizontal convergence (equal to the convergence calculated at 400 m) is assumed below $z = 400$ m AGL, the lowest grid level at which the objectively analyzed velocity observations from both radars provide adequate data coverage within the rear and forward flanks of the storm for verification. The dual-Doppler syntheses reveal certain low-level features such as the vorticity maximum associated with the mesocyclone and the rear- and forward-flank downdrafts and gust fronts, all of which qualitatively resemble those retrieved using a finer grid spacing and slightly different objective analysis criteria (Markowski et al. 2012a,b; Kosiba et al. 2012; Richardson et al. 2012).

The EnKF and dual-Doppler methods produce similar values and trends of vertical vorticity, similar qualitative patterns of vertical velocity and horizontal convergence/divergence along the gust fronts and in the rear-flank downdraft, and similar orientations of the horizontal wind and three-dimensional vorticity vectors. There is an area of enhanced horizontal vorticity located in the storm inflow 5–15 km east-southeast of the vertical vorticity maximum near the time of tornadogenesis (e.g., Fig. 13b). It is plausible that this is a realistic feature when considering simulations shown by Brooks et al. (1994), who found helicity enhancements in regions of enhanced inflow. However, owing to ground clutter contamination, no dual-Doppler data are available in this area to further evaluate this feature.

Though the qualitative patterns of the EnKF and dual-Doppler kinematic fields are similar, there are some differences in the magnitudes of the vertical motion and the horizontal vorticity vectors. Slight differences in regions having dual-Doppler coverage could stem from either

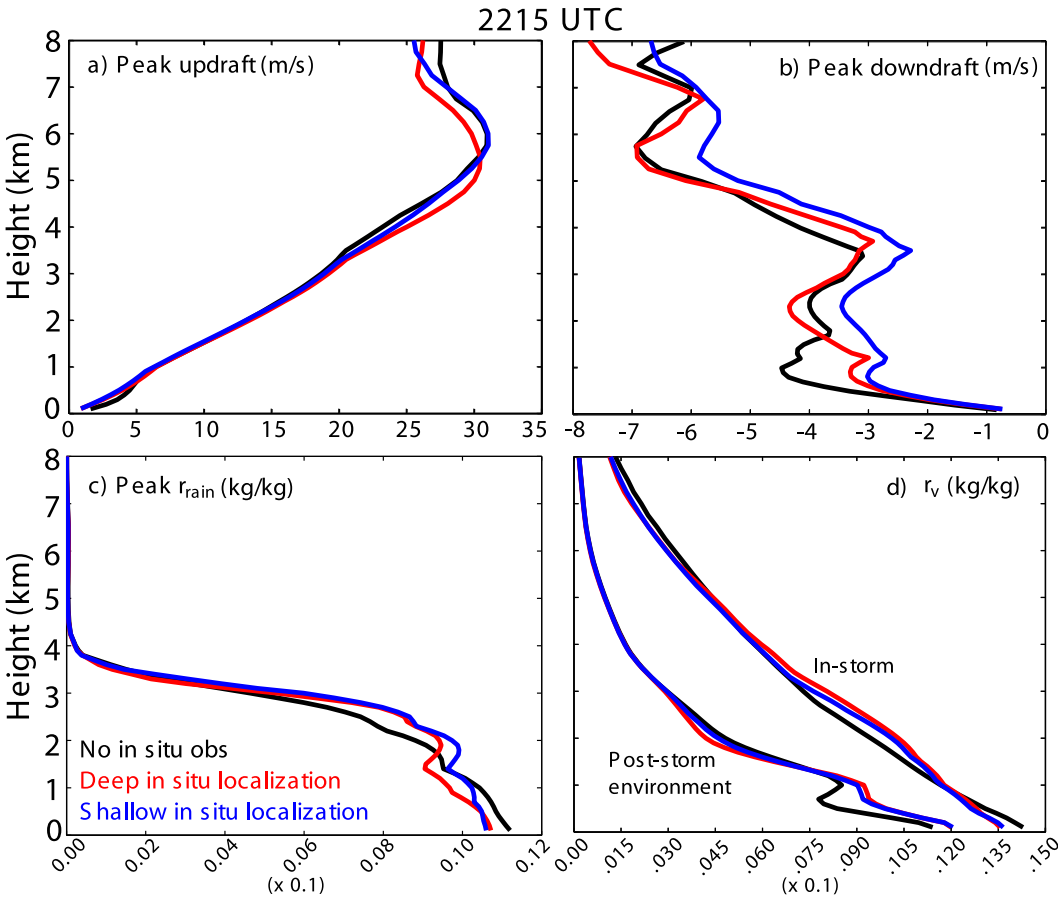

FIG. 9. Vertical profiles of (a) peak vertical velocity, (b) minimum vertical velocity, (c) peak rainwater mixing ratio near the mesocyclone, and (d) water vapor mixing ratio approximately 10 km west of the precipitation core (i.e., in the precipitation-free "poststorm environment") and within the updraft core ("in storm"). Profiles are taken from 1-km sensitivity experiments in which no mobile mesonest observations are assimilated (black), and mobile mesonet observations are assimilated with a vertical localization that reduces to zero at 6 km (blue) and 18 km (red).

data assimilation or the dual-Doppler methodology, such as the quality of the fit of the assimilated observations or the assumed extrapolation below the radar horizon in the dual-Doppler analysis. The evaluation of the many sources of error stemming from assumptions in the dual-Doppler wind synthesis methodology, which considered as an ensemble of possible wind solutions would provide error statistics for the method, is beyond the scope of this study. However, the dual-Doppler winds calculated herein generally fit within the range of ensemble forecasts (e.g., Fig. 14). Possibly the worst fit of the dual-Doppler winds to the ensemble occurs in the near-storm inflow environment, where dual-Doppler u and w are at least three ensemble standard deviations from the ensemble mean (differences of 0.6–2 m s^{-1} and small ensemble spread in this region exaggerate a poor fit of the dual-Doppler w to the model ensemble). Dual-Doppler winds also differ from the forecast ensemble within the rear-flank downdraft region and surrounding the surface gust fronts owing to differences in relative magnitudes and slight spatial displacements of peak low-level updrafts/downdrafts. Potvin and Wicker (2012) compare the accuracy of dual-Doppler and EnKF analyses throughout the depth of a storm, using a model reference solution as truth, for various assumed radar beam crossing angles and data availability. We compare dual-Doppler syntheses to EnKF analyses at times when the best dual-Doppler data are available (i.e., the times with the best beam crossing angles). From their findings, it is possible that the EnKF kinematic analyses could be degraded slightly at times when fewer radars are available, such as after DOW7 undeploys at 2218 UTC. Although, two mobile radars and KCYS are assimilated during this time with beam crossing angles sufficient for dual-Doppler synthesis, radar deployment geometry provides a relatively high dual-Doppler data horizon (between DOW6 and NOXP) compared to earlier times.

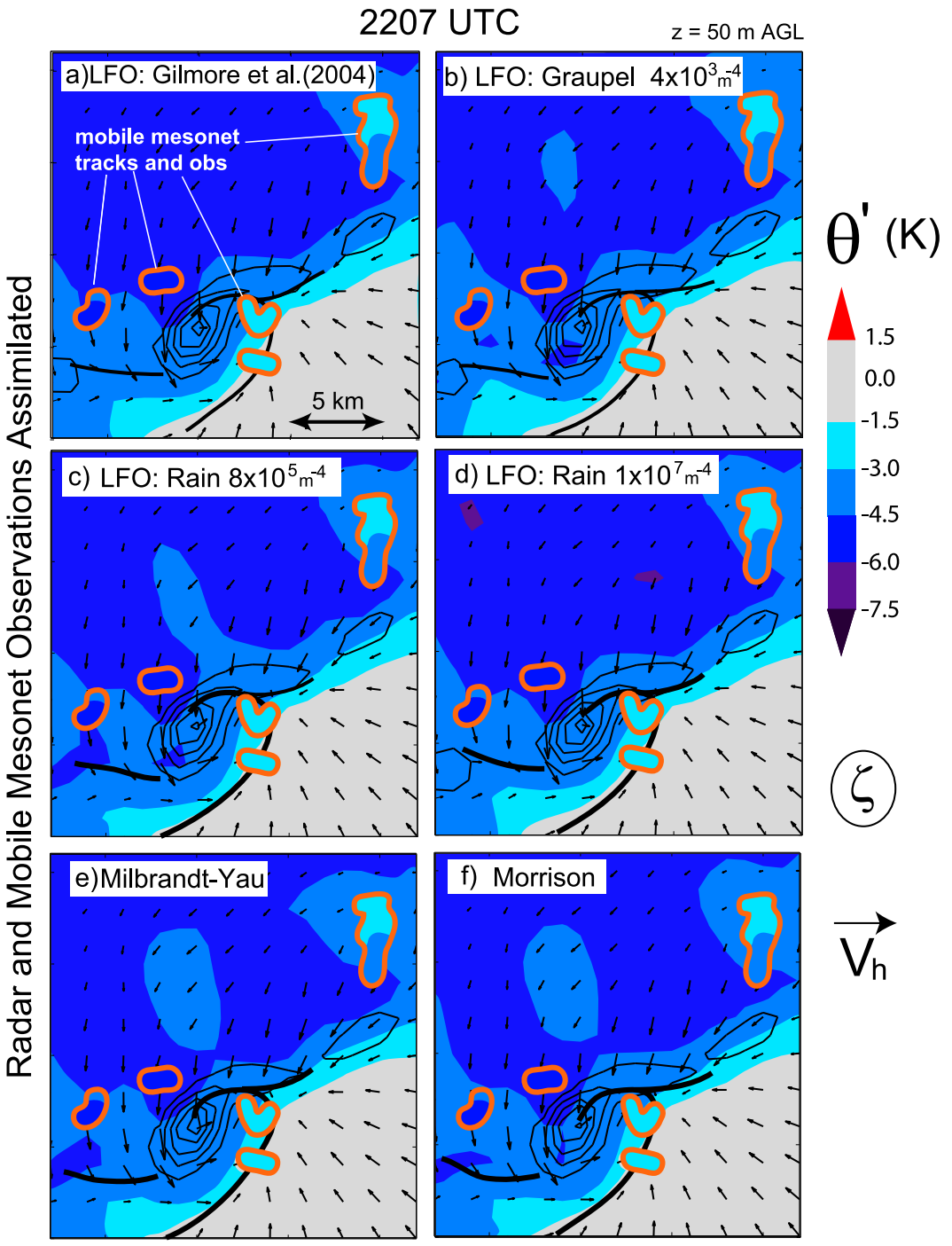

FIG. 10. As in Fig. 5, but for experiments that also assimilate mobile mesonet θ and q_v observations.

b. Thermodynamic analyses

Because horizontal buoyancy gradients and their associated horizontal vorticity generation are presumed to be important to the development of rotation near the surface (e.g., Rotunno and Klemp 1985; Davies-Jones and Brooks 1993), their validity in the EnKF analyses is of great interest. Figure 15 shows the differences between mobile mesonet surface observations of r_v, virtual potential temperature θ_v, equivalent potential temperature θ_e, and EnKF analyses of these variables interpolated to the storm-relative locations of each mobile

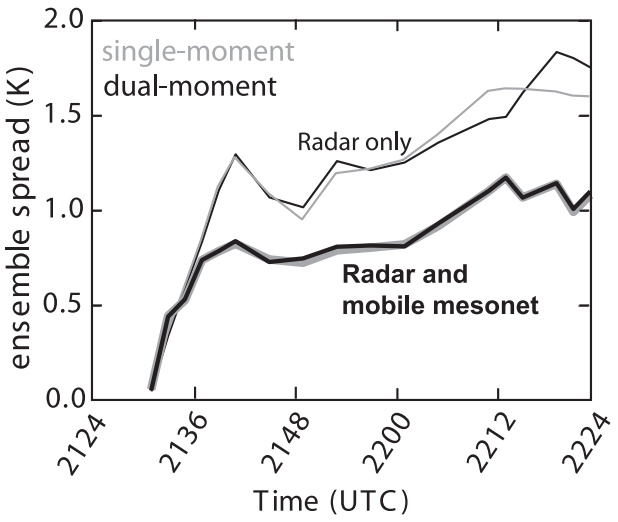

FIG. 11. Forecast (prior) ensemble standard deviation of θ in observation space from four experiments that are identical except for the microphysics parameterization [black lines represent experiments using the dual-moment Morrison et al. (2005) scheme, the gray lines show the single-moment LFO scheme with graupel and rain intercept parameters of $4 \times 10^4\,\mathrm{m}^{-4}$ and $8 \times 10^6\,\mathrm{m}^{-4}$, respectively], and the observation type that is assimilated (thin lines represent experiments assimilating only radar velocities, thick lines are from experiments assimilating radar velocities and mobile mesonet θ and q_v observations).

mesonet observation collected mostly in the outflow air. Figure 16 shows overlays of mobile mesonet observations on the ensemble-mean cold pool at $z = 50$ m AGL. The largest difference between the r_v observations and EnKF analyses during the experiment is about $2.5\,\mathrm{g\,kg}^{-1}$, but is more typically $<1\,\mathrm{g\,kg}^{-1}$, with an overall average near zero. The maximum difference in the θ_v field is about 3 K, but on average, the ensemble-mean θ_v is about 0.5 K cooler than the observations. Differences in observed and EnKF θ_v and r_v analyses yield differences in the observed and EnKF θ_e analyses as large as 6 K, although these differences are most often less than 2 K and average near zero (Figs. 15c and 16g–i). Overall, the greatest differences between the EnKF analyses and observations in the cold pool are located in the western rear-flank region of the storm (e.g., >5 km west-northwest of the mesocyclone center) shortly after the ensemble spinup period during which the 2130 UTC DOW7 volume is repeatedly assimilated (e.g., Figs. 16a,d,g). The large θ_v differences in this area of the storm generally decrease in time (Figs. 16a–c), suggesting increasing reliability of the EnKF temperature analyses during and after tornadogenesis. There are occasional warm and moist or cold and dry anomalies in the θ_v and r_v fields near the mesocyclone throughout the experiment that sometimes differ from the observations by as much as 3.0 K and $1.5\,\mathrm{g\,kg}^{-1}$ (e.g., cold and dry pockets within and east of the mesocyclone in Figs. 16a–f). Similar anomalies have arisen in most of our experiments regardless of whether mobile mesonet observations are assimilated; they are highly sensitive to the model grid resolution and slightly sensitive to the choice of model microphysics schemes and the method for the maintenance of ensemble spread. Figure 17 shows how the assimilated in situ observations from two mobile mesonet probes compare to the forecasted ensemble spread at locations throughout the storm. Most in situ observations are within one standard deviation of the ensemble mean. A notable exception is when the mobile mesonets enter a cold and dry anomaly in the rear-flank outflow near the mesocyclone (e.g., between 2201 and 2211 UTC in Figs. 17b,d). There is an increase in the forecasted ensemble spread in this location of the storm.

Gridded radar reflectivity from the KCYS WSR-88D is compared to the 10-cm radar reflectivity calculated from the 500-m-resolution ensemble-mean hydrometeor fields at $z = 1.5$ km in Fig. 18. The reflectivity fields capture similar bulk features, such as a peak reflectivity core north-northeast of the vorticity maximum, horizontal fanning of smaller precipitation particles downstream of the updraft, and a hook echo around the mesocyclone. However, the EnKF-retrieved maximum reflectivity is roughly 8–10 dB larger than that collected by the KCYS radar. Additionally, the EnKF hook echo sometimes is less clearly defined and contains more precipitation than is depicted by the WSR-88D. There is only a small sensitivity of these structures to the model microphysics schemes used with a coarser (1 km) model grid spacing.

c. *Trajectory calculations and Lagrangian vorticity budgets*

In Part II, a variety of parcel trajectories are calculated using EnKF wind fields to evaluate the airflow surrounding the mesocyclone within the rear-flank downdraft outflow and within the primary midlevel updraft. Here, we evaluate the veracity of EnKF backward (in time) trajectories for 20 parcels, located along a ring with a radius of 1 km centered on the low-level mesocyclone, by comparing them to trajectories calculated using dual-Doppler observations (Fig. 19). Parcel trajectories are calculated using the EnKF or dual-Doppler velocity fields available every 2 min with a fourth-order Runge–Kutta scheme and a 10-s time step. The trajectories are computed within the storm-relative reference frame (using a mean midlevel updraft motion) to minimize temporal interpolation errors caused by the motion of storm features. Because of our conservative constraints designed to prevent extrapolation in the dual-Doppler

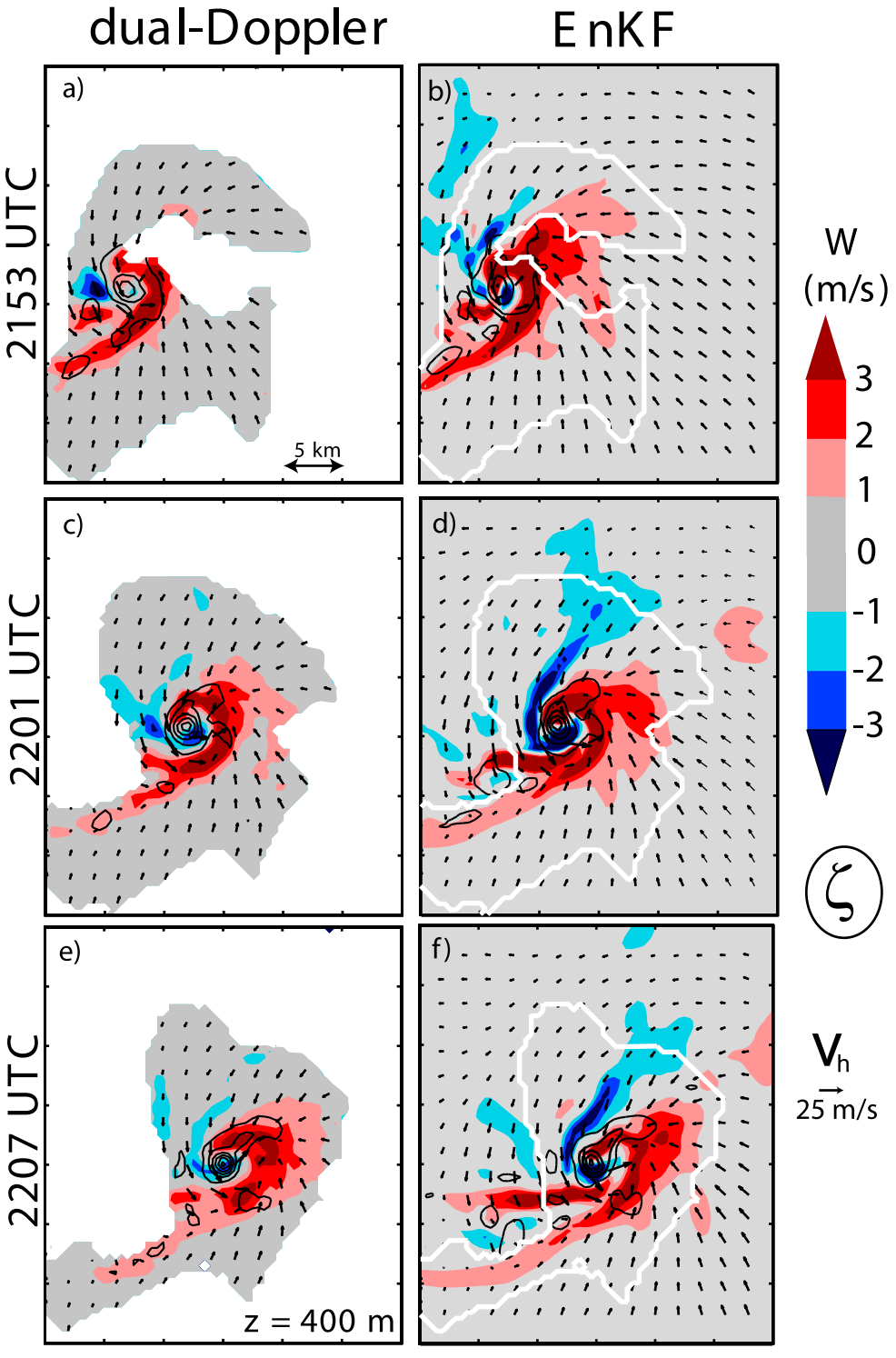

FIG. 12. (right) A sequence of EnKF analyses of ground-relative horizontal wind (vectors), vertical velocity (shaded), and vertical vorticity (contours; outermost contour is 0.003 s^{-1}, incremented by 0.01 s^{-1}) calculated from the ensemble-mean u and v fields at 2153, 2201, and 2207 UTC at z = 400 m AGL. (left) Dual-Doppler syntheses of the same kinematic fields in the right column valid at the same times and plotted within the same portion of the model domain. White areas in the left column indicate regions of missing dual-Doppler data and white contours in the right column indicate the horizontal edge of the dual-Doppler coverage overlaid on the EnKF domain.

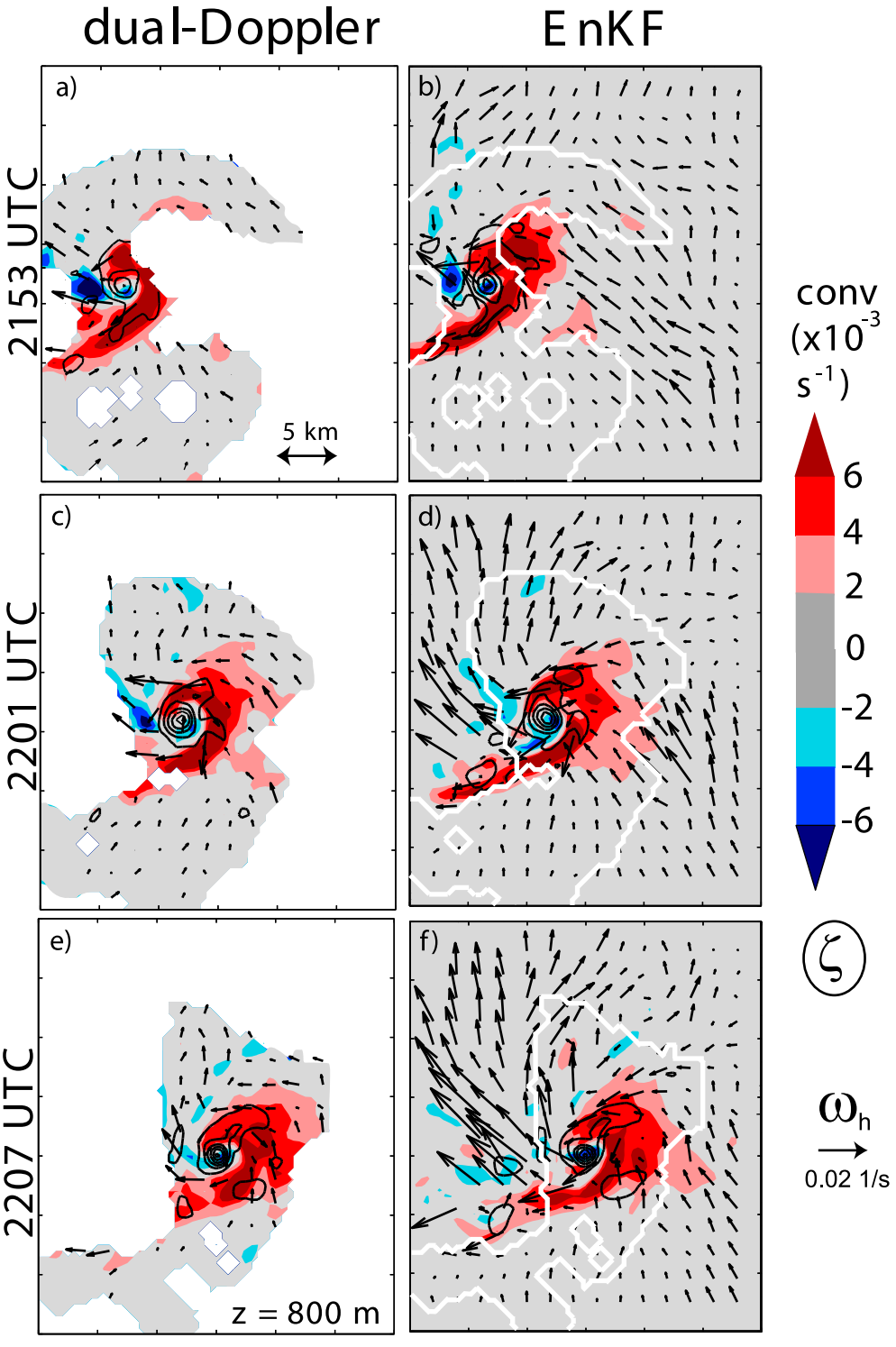

FIG. 13. As in Fig. 12, but with horizontal vorticity (vectors) and horizontal convergence (shaded) at $z = 800$ m AGL.

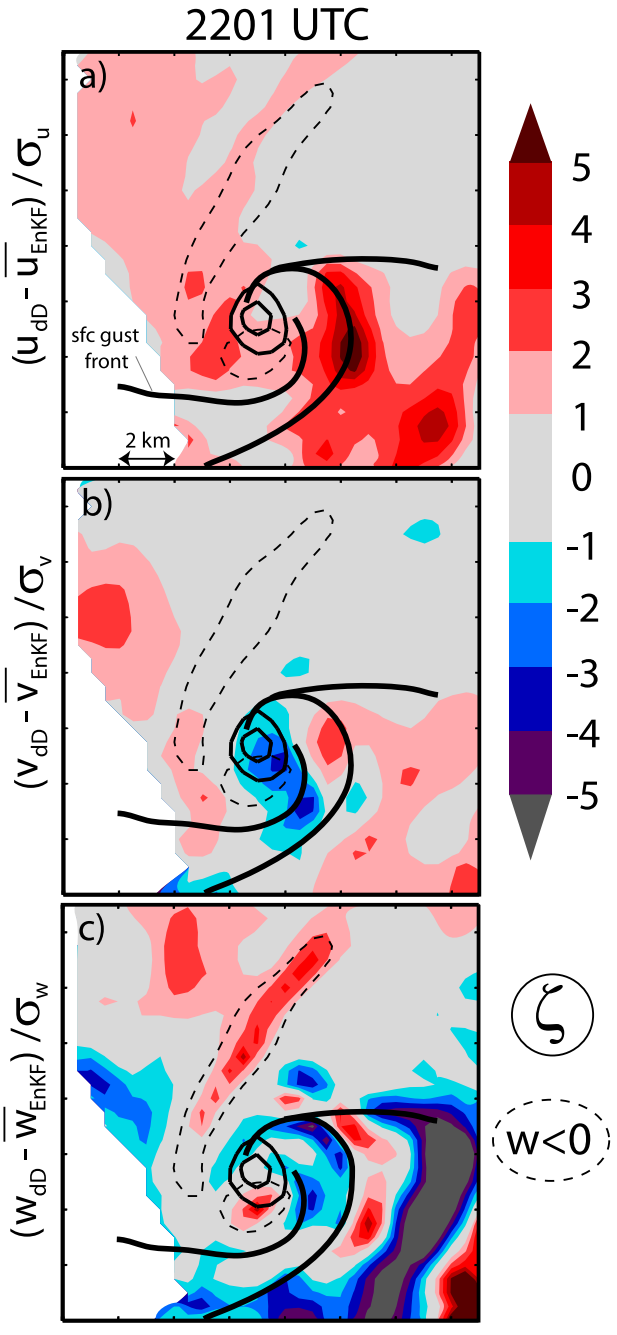

FIG. 14. Difference between dual-Doppler and forecast ensemble-mean u, v, and w at 2201 UTC and $z = 400$ m, normalized by the spatially varying ensemble standard deviation. Ensemble-mean $w = -2\,\mathrm{m\,s^{-1}}$ (black dashed contours), $\zeta = 0.02$ and $0.03\,\mathrm{s^{-1}}$ (black contours), and traces of the low-level updraft along the gust fronts (thick black lines) are overlaid.

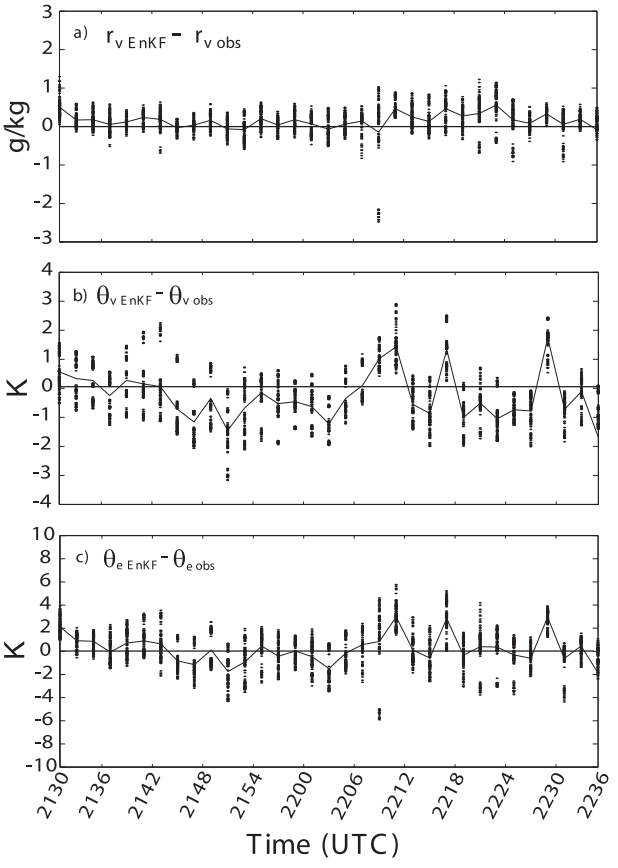

FIG. 15. Differences between mobile mesonet observations of (a) r_v, (b) θ_v, and (c) θ_e, and the values computed from ensemble-mean analyses interpolated to the positions of the mobile mesonets as a function of time. The difference between each observation and the ensemble-mean value is shown as one dot at each EnKF analysis time. The average of these differences at each time is traced with a solid line.

wind syntheses, it was difficult to find a period in the dual-Doppler data that would allow us to track many of the parcels in the ring backward for a long period of time before reaching the edges of the observations. The trajectory calculations in Fig. 19 are from parcels that originate at $z = 700$ m at 2211 UTC, a location and a time chosen to provide the largest amount of four-dimensional dual-Doppler data for continuous backward trajectories.

The majority of the parcels en route to the low-level mesocyclone in the EnKF analyses originate near the ground, many ascending to $z \geq 1500$ m AGL before descending into their positions in the ring at 700 m. Qualitatively similar parcel paths have been inferred near the time of tornado or mesocyclone maturity from past observations or modeling studies (e.g., Brandes 1981; 1984; Wicker and Wilhelmson 1995; Wakimoto and Liu 1998; Dowell and Bluestein 2002; Mashiko et al. 2009; Noda and Niino 2010; Dahl et al. 2012). Some of the parcels coming from the inflow environment follow paths toward the mesocyclone that do not traverse the forward flank. They appear to penetrate the rear-flank

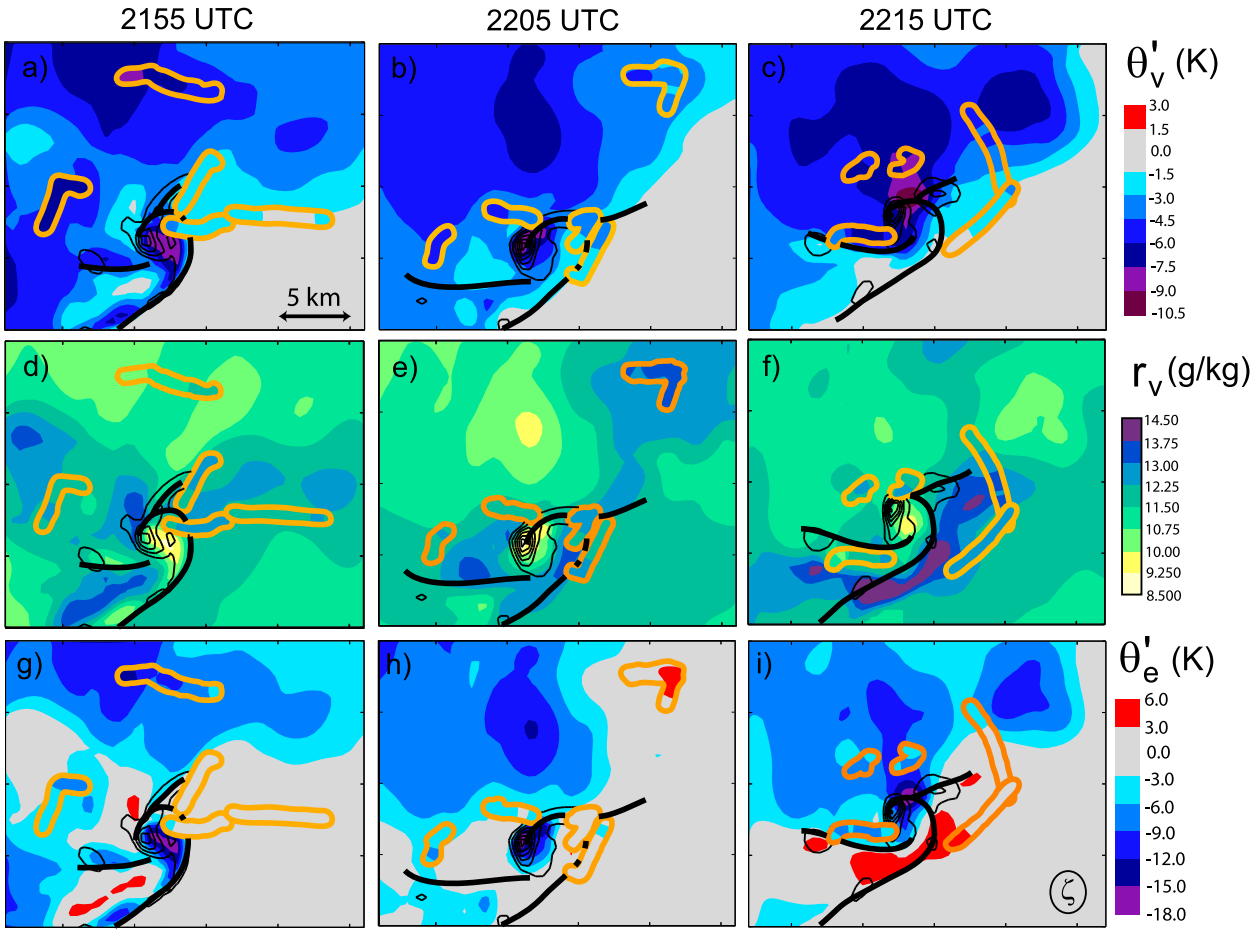

FIG. 16. Ensemble-mean (a)–(c) θ'_v, (d)–(f) r_v, and (g)–(i) θ'_e analyses at the lowest model scalar grid level at 2155, 2205, and 2215 UTC. Vertical vorticity is contoured in black (outermost contour is $0.003\,s^{-1}$, incremented by $0.005\,s^{-1}$) and the low-level updraft maximum along the gust fronts is traced with a thick black line. Time-to-space-converted mobile mesonet observations of θ'_v, r_v, and θ'_e valid within 2 min of the EnKF analysis time are overlaid (orange swaths with observations color-filled).

outflow at an angle nearly perpendicular to the gust front plane (e.g., the southernmost five trajectory paths in Fig. 19b). These unexpected paths are due to differences in the motions of individual storm features compared to the reference mean updraft motion during the trajectory integration period and are, therefore, an illusion of plotting the storm-relative trajectories at one analysis time. In reality (i.e., when the trajectories are viewed in a series of ground-relative plots), these parcels pass through the inflow notch on the northern periphery of the mesocyclone, roughly paralleling the rear-flank gust front as they wrap cyclonically around the center of rotation. However, Dahl et al. (2012) noted that backward trajectories entering the low-level mesocyclone almost directly from the inflow environment appeared to be an artifact of coarse temporal resolution because more accurate forward trajectories computed during the model run time with a finer time step did not follow the same paths. It is possible that some of our trajectories suffer from similar errors and must be interpreted with care. Though dual-Doppler trajectories are comparatively short because of the limited dual-Doppler coverage, the EnKF and dual-Doppler trajectories qualitatively match motions around the mesocyclone, some of which traverse the forward-flank region of the storm. Markowski et al. (2012a,b) and Kosiba et al. (2012) show qualitatively similar trajectories at other times during the intercept of this storm using different spatial resolutions and dual-Doppler synthesis methodology.

To further assess how processes leading to the evolution of the three-dimensional vorticity vector are captured by the EnKF ensemble-mean analyses, a calculation of the Lagrangian three-dimensional vorticity budget is performed along various parcel trajectories using

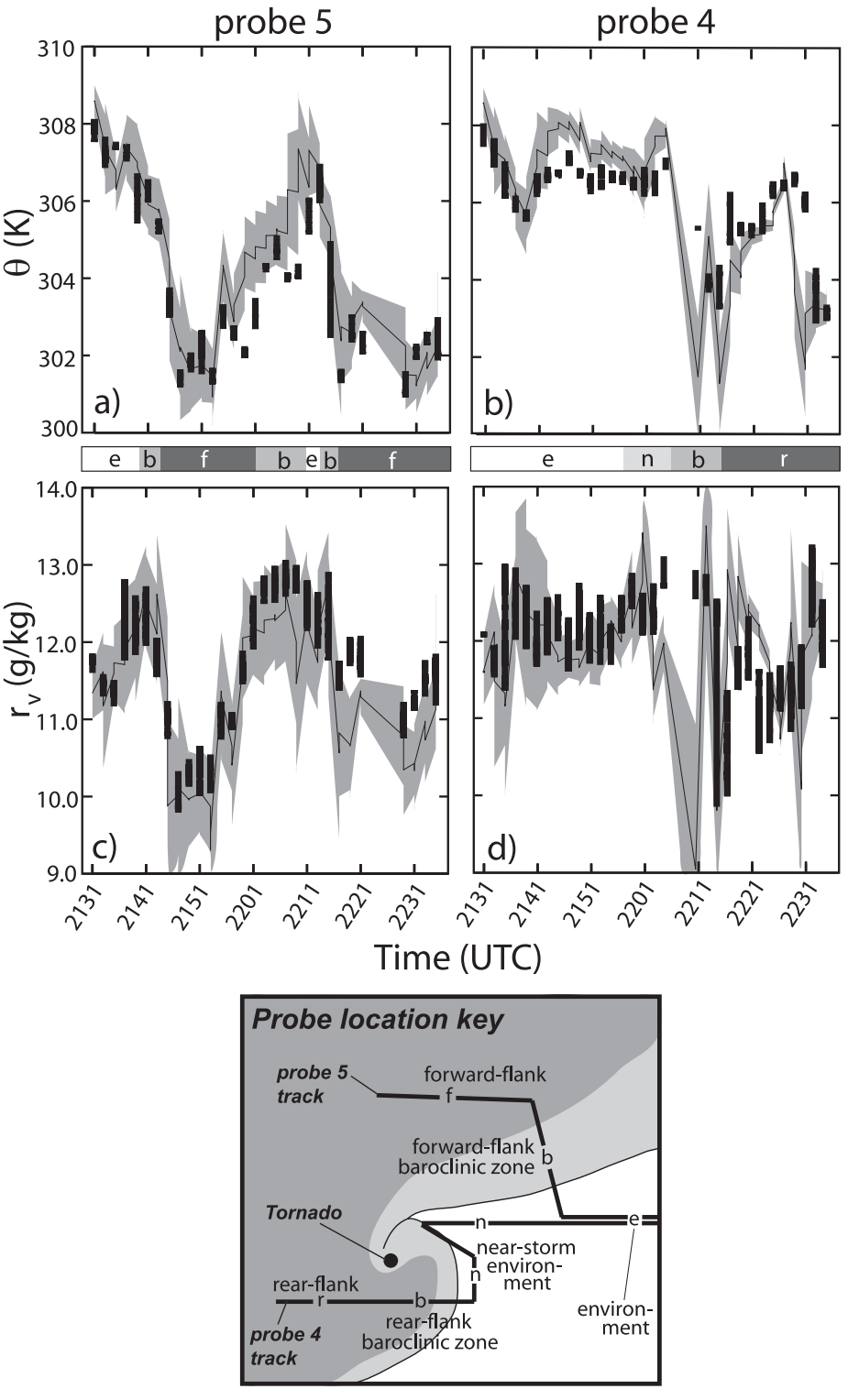

FIG. 17. Comparisons of (a),(b) θ and (c),(d) r_v observations collected by two mobile mesonets [probes (right) 4 and (left) 5; thick black vertical bars represent the range of values at each analysis time] to the forecast (prior) ensemble mean (thin black line) and forecast ensemble spread (gray swath represents values within one standard deviation of the ensemble mean). The shaded bar between (a),(c) and (b),(d) labels the approximate storm-relative locations of probes 4 and 5 (shown by e, b, f, n, and r). (bottom) Schematic of the tracks of these two mesonet probes relative to the tornado, cold pool, and environmental air, providing a key to interpret these labels.

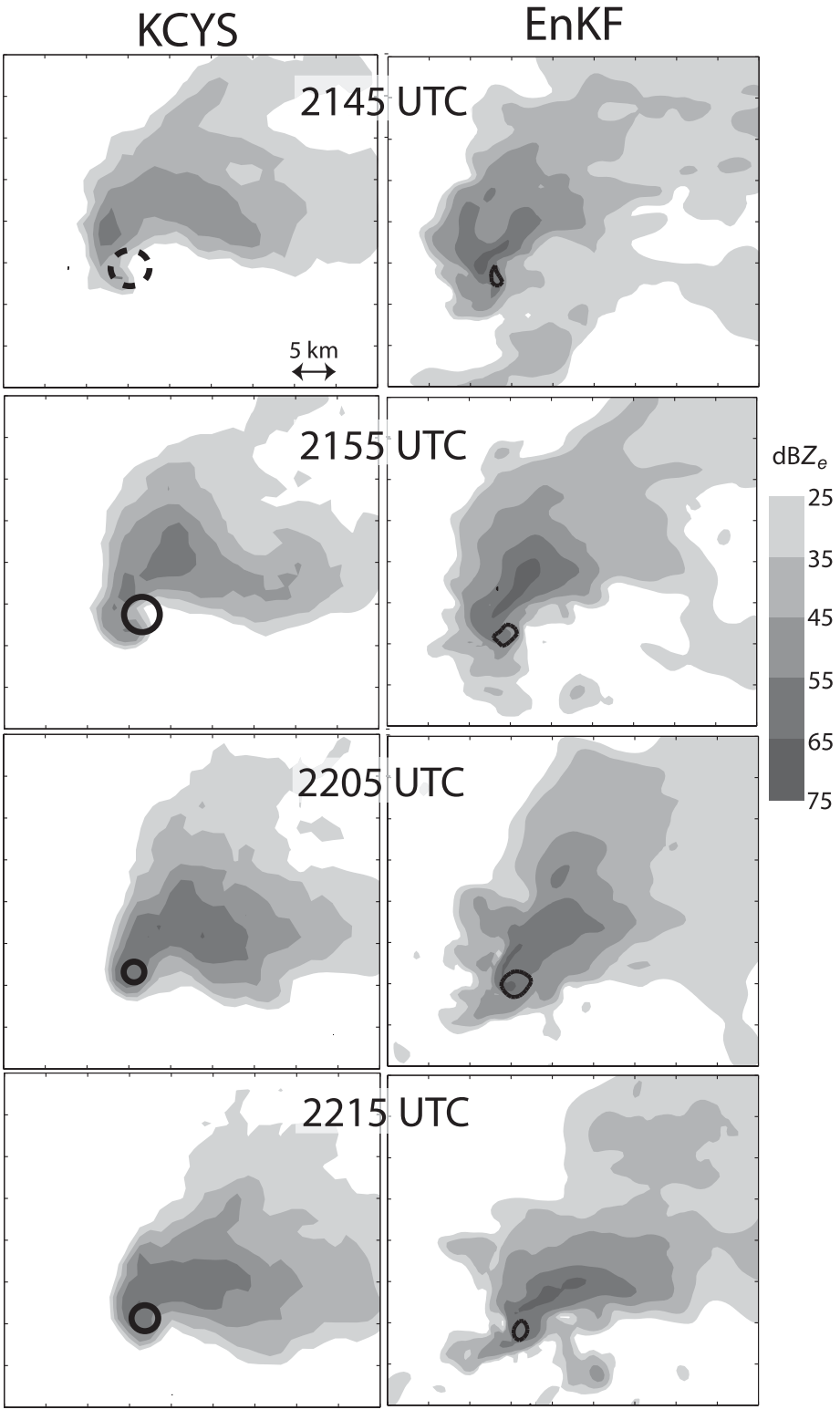

FIG. 18. (left) Gridded KCYS radar reflectivity and (right) 10-cm radar reflectivity calculated from ensemble-mean hydrometeor fields at z = 1.5 km AGL at four times (2145, 2155, 2205, and 2215 UTC). (right) Ensemble-mean vertical vorticity of 0.01 s^{-1} is contoured and (left) the approximate size and position of the KCYS radar velocity couplet is shown with black rings at z = 1.5 km AGL at each time. (top left) The dashed circle indicates that there is uncertainty in the size of the mesocyclone in the KCYS radial velocity data.

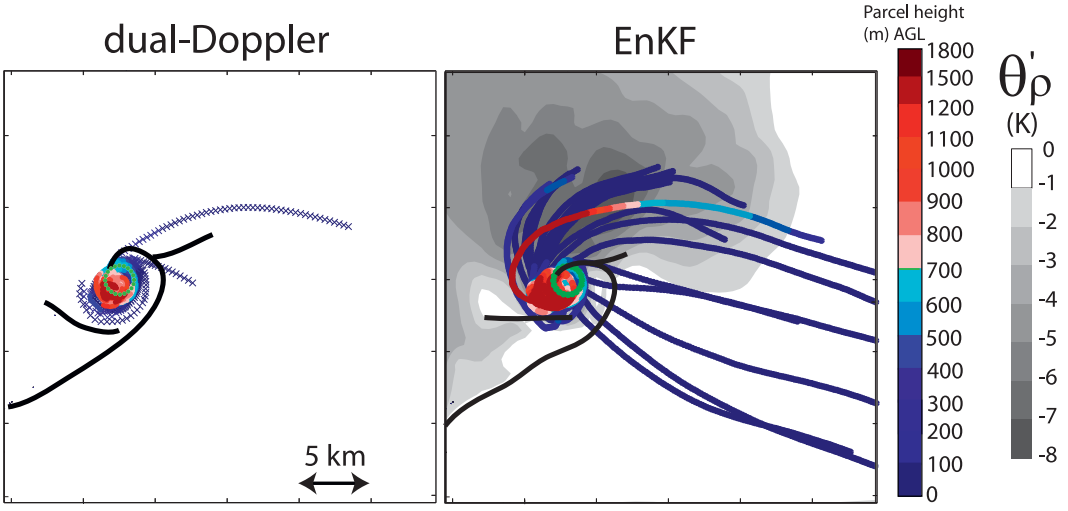

FIG. 19. Storm-relative horizontal positions of 20 parcels initially located at $z = 700$ m AGL and 1-km distance from the vertical vorticity maximum at 2211 UTC along their trajectories integrated backward in time. Trajectories are calculated using the (left) dual-Doppler wind syntheses and (right) EnKF ensemble-mean u, v, and w analyses. The color of each dot along the trajectory indicates a parcel's altitude; green dots show the initial positions of the parcels (at 2211 UTC). Parcel positions indicated with an × in the left panel indicate locations along the trajectory where parcels are below 400 m (the radar horizon in the dual-Doppler wind syntheses). The ensemble mean of the perturbation density potential temperature field (shaded) at $z = 200$ m AGL at 2211 UTC is also shown. The low-level updraft maximum along the gust fronts is traced with a black line.

$$\xi(t) = \xi_0 + \int_{t_0}^{t} \left(\eta \frac{\partial u}{\partial y} + \zeta \frac{\partial u}{\partial z} + \xi \frac{\partial u}{\partial x} + \frac{\partial B}{\partial y} \right) dt',$$

$$\eta(t) = \eta_0 + \int_{t_0}^{t} \left(\xi \frac{\partial v}{\partial x} + \zeta \frac{\partial v}{\partial z} + \eta \frac{\partial v}{\partial y} - \frac{\partial B}{\partial x} \right) dt',$$

$$\zeta(t) = \zeta_0 + \int_{t_0}^{t} \left(\xi \frac{\partial w}{\partial x} + \eta \frac{\partial w}{\partial y} + \zeta \frac{\partial w}{\partial z} \right) dt', \qquad (1)$$

where (ξ, η, ζ) is the three-dimensional vorticity vector at the parcel location, (ξ_0, η_0, ζ_0) is the three-dimensional vorticity vector at the beginning time of the trajectory (i.e., the final time in the backward parcel trajectory calculation), $B = g(\theta_\rho - \overline{\theta_\rho})/\overline{\theta_\rho}$, θ_ρ is the density potential temperature (Emanuel 1994) of the parcel, and $\overline{\theta_\rho}$ is the environmental density potential temperature taken from the model base state at each height. The first two terms on the rhs of each component represent tilting, the third term represents stretching, and the fourth term (ξ and η equations) represents baroclinic production of horizontal vorticity. These equations are derived from the inviscid[3] and Boussinesq momentum equations in the absence of planetary rotation. Ensemble-mean values of θ_ρ, u, v, and w are used to compute ξ, η, ζ, and B.

[3] Turbulent mixing is neglected owing to the difficulty of its estimation from the ensemble-mean flow fields.

A sample Lagrangian vorticity budget is calculated for a parcel that originates in the inflow, traverses the baroclinic zone on the forward flank of the storm, and descends within the rear-flank downdraft into the outer edges of the mesocyclone ($\zeta \sim 0.004\,\mathrm{s}^{-1}$) at $z = 200$ m (Fig. 20a). This rear-flank downdraft parcel is chosen because it travels through areas of the storm of interest for examination in Part II of this study, it typifies many of its neighbors, and it remains above the lowest model scalar grid level for a substantial period. This latter constraint is applied in order to eliminate potential errors introduced by assumptions necessary when the trajectory drops below the lowest scalar level. Values of ξ, η, and ζ computed along the parcel trajectory with (1) are compared to the ensemble-mean values of ξ, η, and ζ interpolated from the model grid to the parcel location. A close match between the two indicates a realistic evolution in the ensemble-mean analyses, bolstering confidence in our use of them to evaluate storm dynamics.

Computations of (1) are performed with and without the baroclinic generation term to perhaps further verify that our four-dimensional thermodynamic structure is dynamically consistent with the kinematic analyses (Fig. 20b). Trends of interpolated and integrated (with baroclinic generation) ξ and η are qualitatively similar, and differences between interpolated and integrated ξ and η are typically smaller when the baroclinic generation term is included as opposed to when it is excluded. The

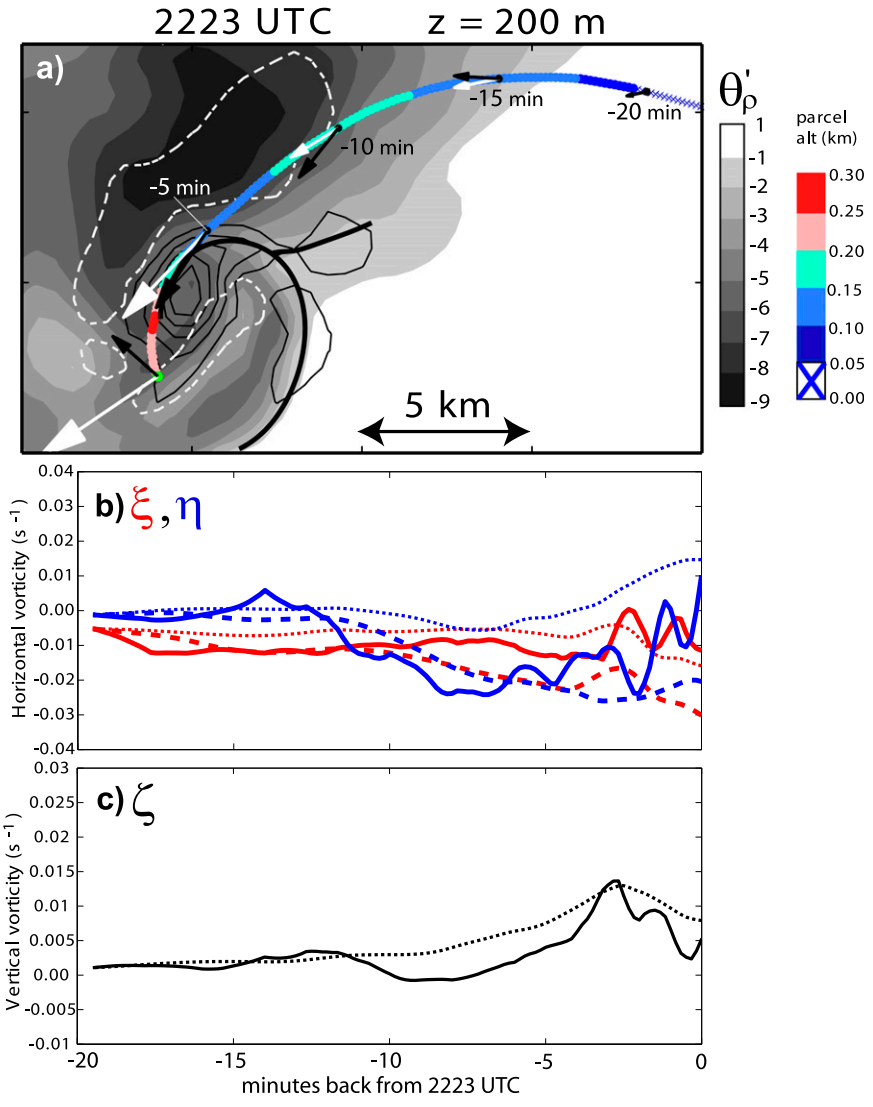

FIG. 20. (a) Horizontal positions of a parcel integrated backward in time from a location in the rear-flank downdraft at $z = 200$ m AGL at 2223 UTC. The parcel positions (dots with colors indicating their altitude) are overlaid on the ensemble-mean perturbation density potential temperature field (shaded), vertical vorticity (thin contours; outermost contour is $0.003\,s^{-1}$, incremented by $0.003\,s^{-1}$), $w = -1\,m\,s^{-1}$ (white dashed contour), and traces of the updraft maximum along the gust fronts (thick lines) at $z = 200$ m at 2223 UTC. Blue ×s along the parcel trajectory indicate that the parcel is located below the lowest model scalar grid level ($z = 50$ m). Times backward from 2223 UTC are indicated along the trajectory in 5-min increments. Ensemble-mean horizontal vorticity and the horizontal vorticity calculated by integrating (1) along the trajectory are shown with black and white vectors, respectively, at 5-min increments. (b),(c) Ensemble-mean ξ, η, and ζ interpolated to the trajectory (solid red, blue, and black lines, respectively) and calculated using (1) (dashed lines) for the parcel in the top panel. Calculations of (1) are performed with $\xi_0 = \xi\,(t = -19\,\text{min})$, $\eta_0 = \eta\,(t = -19\,\text{min})$, and $\zeta_0 = \zeta\,(t = -19\,\text{min})$ and terms are integrated forward in time to $t = 0$ min. Dotted red and blue lines represent ξ and η computed using (1) without the baroclinic generation terms.

latter fact may further indicate that the thermodynamic and kinematic analyses in the area of the storm traversed by this and similar parcel trajectories are realistic. Though there are differences of up to $0.015\,s^{-1}$ between the ensemble-mean and integrated (with baroclinic terms) values of ξ along the trajectory, overall, the three-dimensional vorticity signals match most closely between $-19 < t < -5$ min, when the parcel traverses

the forward-flank region. During this period, the differences between ensemble-mean and integrated ξ and η are comparatively small. Accordingly, although the ensemble-mean and integrated horizontal vorticity vectors contain quantitative differences along the trajectory during this time, they have similar orientations and magnitudes (black and white vectors in Fig. 20a), resembling those expected from baroclinic generation traditionally observed in this region of a supercell. Though there are sometimes differences as large as $0.005\,s^{-1}$ for ζ, integrating (1) qualitatively captures the trend up to a similar peak value at $t = -3$ min, and the subsequent decrease. Ensemble-mean and integrated ξ and η values disagree most when the parcel is located near the mesocyclone ($-5 < t < 0$ min). This may be partly due to the relatively coarse temporal resolution of the EnKF analyses, which may amplify interpolation errors in the trajectory calculations in regions having strong gradients in the wind field (e.g., Dahl et al. 2012). The fact that the differences between the ensemble mean and integrated vorticity are much smaller within the forward-flank region, where velocity gradients are much smaller, is perhaps consistent with this conclusion. It also is possible that such large differences along this portion of the trajectory are at least partially due to the neglect of turbulent mixing terms in (1), which could be significant within or along the edge of the mesocyclone. These error characteristics suggest that an evaluation of the terms in (1) may provide meaningful information for the evaluation of dynamic processes in certain portions of the storm, but that caution should be used in their interpretation in areas of strong velocity gradients where errors could be substantial.

5. Summary and conclusions

High-resolution mobile Doppler radar velocity and in situ surface observations collected in a tornadic supercell occurring on 5 June 2009 in Goshen County, Wyoming, during VORTEX2 were assimilated into an idealized WRF simulation of a convective storm using the ensemble Kalman filter. Our aim was to generate a sequence of ensemble analyses capturing a realistic evolution of the supercell that can be used to study the mesocyclone-scale processes associated with tornado formation, maintenance, and demise. These processes will be evaluated in Part II of this study.

The focus of the present paper is on determining how well the EnKF analyses captured a realistic evolution of the Goshen County supercell. Prior to performing our highest-resolution EnKF experiments, we evaluated the sensitivity of outflow characteristics to the assimilation of mobile mesonet potential temperature and moisture observations within the context of different localization radii and microphysics schemes. Using our high-resolution (500-m grid spacing) analyses, we compared the EnKF analyses and parcel trajectories computed from them to those from dual-Doppler wind syntheses. Finally, we examined the credibility of calculating Lagrangian three-dimensional vorticity budgets that could be used to evaluate the development of low-level rotation. Our primary findings can be summarized as follows:

1) The assimilation of large quantities of radar velocity data produces ensemble-mean u, v, w, and ζ fields that qualitatively resemble dual-Doppler wind syntheses; thus, a realistic evolution of the mesocyclone, gust fronts, downdraft, inflow, and horizontal vorticity appears to be portrayed by the EnKF analyses.
2) The assimilation of mobile mesonet thermodynamic data reduces the variability of outflow coldness that can arise owing to the choice of model microphysics schemes, reducing the uncertainty in the analysis within the cold pool based on such choices.
3) Precipitation analyses (using EnKF reflectivity as a proxy) portray a precipitation structure similar to the classic supercell structure depicted by the nearest WSR-88D, but contain larger simulated peak radar reflectivity values and a hook echo that sometimes contains more precipitation than is found in reality.
4) Lagrangian three-dimensional vorticity budgets integrated along several trajectories match qualitatively well with values of ensemble-mean vorticity interpolated to each parcel location in areas of the storm containing relatively small velocity gradients.

Our highest confidence in the EnKF analysis variables lies with the kinematic fields owing to their resemblance to dual-Doppler observations. Quantitative differences between the dual-Doppler and EnKF kinematic fields likely arise owing to uncertainty in model parameterizations *and* assumptions in the dual-Doppler methodology; therefore, it is unclear which method is closer to the truth. We also are confident in the near-surface thermodynamic analyses in the cold pool because of the relative lack of sensitivity to the tested model microphysical schemes and a seemingly beneficial impact on the ensemble thermodynamic fields despite a simplified modeling environment. Unfortunately, no in situ observations are available above the ground in this storm to verify EnKF thermodynamic fields aloft. It should be reiterated that data collection errors are inherent to all observation platforms, so neither the observations nor the EnKF analyses can be considered the truth. However, we believe there is sufficient agreement between trends in low-level modeled and observed buoyancy fields to permit a reasonably confident evaluation of

trends in cold pool characteristics. Long parcel residence times within the mesocyclone, where larger velocity gradients are present, yield larger disagreement between the integrated and interpolated parcel vorticity. Errors in parcel position or integrated forcing terms in the Lagrangian vorticity budget in this area of the storm may be due to the relatively coarse temporal resolution of our analyses and the difficulty in estimating subgrid-scale mixing terms. However, we believe it is possible to perform a meaningful diagnosis of certain mesocyclone-scale processes using the ensemble-mean analyses, keeping all of these caveats in mind.

Acknowledgments. This research was funded by National Science Foundation Grants AGS-0801035, AGS-0801041, AGS-1157646, AGS-1211132, and AGS-0801041, and NOAA's Warn-on-Forecast project. The DOW radars are NSF Lower Atmospheric Observing Facilities supported by AGS-0734001. Data assimilation experiments were conducted using NCAR Yellowstone and CISL facilities, the NCAR Data Assimilation Research Testbed, and the WRF-ARW software packages. We thank Lou Wicker, Jidong Gao, and Altug Aksoy for their helpful comments on this research. We would also like to thank Nancy Collins, Jeff Anderson, Johannes Dahl, Dan Dawson, Hugh Morrison, George Bryan, Chris Snyder, Don Burgess, Pat Skinner, Tony Reinhart, Terra Thompson, Robin Tanamachi, Matt Parker, and Morris Weisman for advice and helpful discussion of topics related to this research. We also are thankful to all participants of VORTEX2 for their dedication in collecting the data used in this study.

REFERENCES

Aksoy, A., D. C. Dowell, and C. Snyder, 2009: A multicase comparative assessment of the ensemble Kalman filter for assimilation of radar observations. Part I: Storm-scale analyses. *Mon. Wea. Rev.,* **137,** 1805–1824.

Anderson, J. L., 2001: An ensemble adjustment Kalman filter for data assimilation. *Mon. Wea. Rev.,* **129,** 2884–2903.

——, 2009: Spatially and temporally varying adaptive covariance inflation for ensemble filters. *Tellus,* **61,** 72–83.

——, T. Hoar, K. Raeder, H. Liu, N. Collins, R. Torn, and A. Avellano, 2009: The Data Assimilation Research Testbed: A community facility. *Bull. Amer. Meteor. Soc.,* **90,** 1283–1296.

Annan, J. D., J. C. Hargreaves, N. R. Edwards, and R. Marsh, 2005: Parameter estimation in an intermediate complexity earth system model using an ensemble Kalman filter. *Ocean Modell.,* **8,** 135–154.

Brandes, E. A., 1977: Flow in severe thunderstorms observed by dual-Doppler radar. *Mon. Wea. Rev.,* **105,** 113–120.

——, 1981: Finescale structure of the Del City–Edmund tornadic mesocirculation. *Mon. Wea. Rev.,* **109,** 635–647.

——, 1984: Vertical vorticity generation and mesocyclone sustenance in tornadic thunderstorms: The observational evidence. *Mon. Wea. Rev.,* **112,** 2253–2269.

Brooks, H. E., C. A. Doswell III, and J. Cooper, 1994: On the environments of tornadic and nontornadic mesocyclones. *Wea. Forecasting,* **9,** 606–618.

Dahl, J. M., M. D. Parker, and L. J. Wicker, 2012: Uncertainties in trajectory calculations within near-surface mesocyclones of simulated supercells. *Mon. Wea. Rev.,* **140,** 2959–2966.

Davies-Jones, R., and H. E. Brooks, 1993: Mesocyclogenesis from a theoretical perspective. *The Tornado: Its Structure, Dynamics, Prediction, and Hazards, Geophys. Monogr.,* Vol. 79, Amer. Geophys. Union, 105–114.

Dawson, D. T. II, M. Xue, J. Milbrandt, and M. K. Yau, 2010: Comparison of evaporation and cold pool development between single-moment and multimoment bulk microphysics schemes in idealized simulations of tornadic thunderstorms. *Mon. Wea. Rev.,* **138,** 1152–1171.

——, L. J. Wicker, and E. R. Mansell, 2012: Impact of the environmental low-level wind profile on ensemble forecasts of the 4 May 2007 Greensburg, Kansas, tornadic storm and associated mesocyclones. *Mon. Wea. Rev.,* **140,** 696–716.

Dowell, D. C., and H. B. Bluestein, 2002: The 8 June 1995 McLean, Texas, storm. Part II: Cyclic tornado formation, maintenance, and dissipation. *Mon. Wea. Rev.,* **130,** 2649–2670.

——, and L. J. Wicker, 2009: Additive noise for storm-scale ensemble data assimilation. *J. Atmos. Oceanic Technol.,* **26,** 911–927.

——, F. Zhang, L. J. Wicker, C. Snyder, and N. A. Crook, 2004: Wind and temperature retrievals in the 17 May 1981 Arcadia, Oklahoma, supercell: Ensemble Kalman filter experiments. *Mon. Wea. Rev.,* **132,** 1982–2005.

——, L. J. Wicker, and C. Snyder, 2011: Ensemble Kalman filter assimilation of radar observations of the 8 May 2003 Oklahoma supercell: Influences of reflectivity observations on storm-scale analyses. *Mon. Wea. Rev.,* **139,** 272–294.

Emanuel, K. A., 1994: *Atmospheric Convection.* Oxford University Press, 580 pp.

Gaspari, G., and S. E. Cohn, 1999: Construction of correlation functions in two and three dimensions. *Quart. J. Roy. Meteor. Soc.,* **125,** 723–757.

Gilmore, M. S., J. M. Straka, and E. N. Rasmussen, 2004: Precipitation and evolution sensitivity in simulated deep convective storms: Comparisons between liquid-only and simple ice and liquid phase microphysics. *Mon. Wea. Rev.,* **132,** 1897–1916.

Jung, Y., M. Xue, and M. Tong, 2012: Ensemble Kalman filter analyses of the 29–30 May 2004 Oklahoma tornadic thunderstorm using one- and two-moment bulk microphysics schemes, with verification against polarimetric radar data. *Mon. Wea. Rev.,* **140,** 1457–1475.

Kosiba, K., J. Wurman, Y. Richardson, P. Markowski, P. Robinson, and J. Marquis, 2012: Genesis of the Goshen County, Wyoming tornado on 5 June 2009 during VORTEX2. *Mon. Wea. Rev.,* **141,** 1157–1181.

Lin, Y., R. D. Farley, and H. D. Orville, 1983: Bulk parameterization of the snow field in a cloud model. *J. Climate Appl. Meteor.,* **22,** 1065–1092.

Markowski, P. M., 2002: Hook echoes and rear-flank downdrafts: A review. *Mon. Wea. Rev.,* **130,** 852–876.

——, J. M. Straka, and E. N. Rasmussen, 2002: Direct surface thermodynamic observations within the rear-flank downdrafts of nontornadic and tornadic supercells. *Mon. Wea. Rev.,* **130,** 1692–1721.

——, ——, and ——, 2003: Tornadogenesis resulting from the transport of circulation by a downdraft: Idealized numerical simulations. *J. Atmos. Sci.,* **60,** 795–823.

——, and Coauthors, 2012a: The pretornadic phase of the Goshen County, Wyoming, supercell of 5 June 2009 intercepted by VORTEX2. Part I: Evolution of kinematic and surface thermodynamic fields. *Mon. Wea. Rev.,* **140,** 2887–2915.

——, Y. Richardson, J. Marquis, J. Wurman, K. Kosiba, P. Robinson, E. Rasmussen, and D. Dowell, 2012b: The pretornadic phase of the Goshen County, Wyoming, supercell of 5 June 2009 intercepted by VORTEX2. Part II: Intensification of low-level rotation. *Mon. Wea. Rev.,* **140,** 2916–2938.

Marquis, J., Y. Richardson, P. Markowski, D. Dowell, and J. Wurman, 2012: Tornado maintenance investigated with high-resolution dual-Doppler and EnKF analysis. *Mon. Wea. Rev.,* **140,** 3–27.

Mashiko, W., H. Niino, and T. Kato, 2009: Numerical simulation of tornadogenesis in an outer-rainband minisupercell of Typhoon Shanshan on 17 September 2006. *Mon. Wea. Rev.,* **137,** 4238–4260.

Milbrandt, J. A., and M. K. Yau, 2005a: A multimoment bulk microphysics parameterization. Part I: Analysis of the role of the spectral shape parameter. *J. Atmos. Sci.,* **62,** 3051–3064.

——, and ——, 2005b: A multimoment bulk microphysics parameterization. Part II: A proposed three-moment closure and scheme description. *J. Atmos. Sci.,* **62,** 3065–3081.

Morrison, H., and J. Milbrandt, 2011: Comparison of the two-moment bulk microphysics schemes in idealized supercell thunderstorm simulations. *Mon. Wea. Rev.,* **139,** 1103–1130.

——, J. A. Curry, and V. I. Khvorostyanov, 2005: A new double-moment microphysics parameterization for application in cloud and climate models. Part I: Description. *J. Atmos. Sci.,* **62,** 1665–1677.

Noda, A. T., and H. Niino, 2010: A numerical investigation of a supercell tornado: Genesis and vorticity budget. *J. Meteor. Soc. Japan,* **88,** 135–159.

Palmer, R., and Coauthors, 2009: Weather education at the University of Oklahoma—An integrated approach. *Bull. Amer. Meteor. Soc.,* **90,** 1277–1282.

Potvin, C. K., and L. J. Wicker, 2012: Comparison between dual-Doppler and EnKF storm-scale wind analyses: Observing system simulation experiments with a supercell thunderstorm. *Mon. Wea. Rev.,* **140,** 3972–3991.

Ray, P. S., C. L. Ziegler, W. Bumgarner, and R. J. Serafin, 1980: Single- and multiple-Doppler radar observations of tornadic storms. *Mon. Wea. Rev.,* **108,** 1607–1625.

Richardson, Y., P. M. Markowski, J. Wurman, K. Kosiba, P. Robinson, and J. Marquis, 2012: The Goshen County, Wyoming, supercell of 5 June 2009 intercepted by VORTEX2: Tornado dissipation phase. Preprints, *26th Conf. on Severe Local Storms,* Nashville, TN, Amer. Meteor. Soc., 6.6. [Available online at https://ams.confex.com/ams/25SLS/webprogram/Paper176231.html.]

Rotunno, R., and J. Klemp, 1985: On the rotation and propagation of simulated supercell thunderstorms. *J. Atmos. Sci.,* **42,** 271–292.

Skamarock, W. C., J. B. Klemp, J. Dudhia, D. O. Gill, D. M. Barker, W. Wang, and J. G. Posers, 2008: A description of the Advanced Research WRF version 3. NCAR Tech. Note TN-468+STR, 88 pp.

Snyder, C., and F. Zhang, 2003: Assimilation of simulated Doppler radar observations with an ensemble Kalman filter. *Mon. Wea. Rev.,* **131,** 1663–1677.

Straka, J. M., E. N. Rasmussen, and S. E. Fredrickson, 1996: A mobile mesonet for finescale meteorological observations. *J. Atmos. Oceanic Technol.,* **13,** 921–936.

Sun, J., and N. A. Crook, 2001: Real-time low-level wind and temperature analysis using single WSR-88D data. *Wea. Forecasting,* **16,** 117–132.

Tanamchi, R. L., L. J. Wicker, D. C. Dowell, H. B. Bluestein, D. T. Dawson, and M. Xue, 2012: EnKF assimilation of high-resolution, mobile Doppler radar data of the 4 May 2007 Greensburg, Kansas, supercell into a numerical cloud model. *Mon. Wea. Rev.,* **141,** 625–648.

Wakimoto, R. M., and C. Liu, 1998: The Garden City, Kansas, storm during VORTEX 95. Part II: The wall cloud and tornado. *Mon. Wea. Rev.,* **126,** 393–408.

Waugh, S., and S. E. Fredrickson, 2010: An improved aspirated temperature system for mobile meteorological observations, especially in severe weather. Preprints, *25th Conf. on Severe Local Storms,* Denver, CO, Amer. Meteor. Soc., P5.2. [Available online at https://ams.confex.com/ams/25SLS/webprogram/Paper176205.html.]

Weiss, C. C., and J. L. Schroeder, 2008: StickNet: A new portable, rapidly deployable surface observation system. *Bull. Amer. Meteor. Soc.,* **89,** 1502–1503.

Wicker, L. J., and R. B. Wilhelmson, 1995: Simulation and analysis of tornado development and decay within a three-dimensional supercell thunderstorm. *J. Atmos. Sci.,* **52,** 2675–2703.

Wurman, J., J. M. Straka, E. N. Rasmussen, M. Randall, and A. Zahrai, 1997: Design and deployment of a portable, pencil-beam, pulsed, 3-cm Doppler radar. *J. Atmos. Oceanic Technol.,* **14,** 1502–1512.

——, D. Dowell, Y. Richardson, P. Markowski, E. Rasmussen, D. Burgess, L. Wicker, and H. Bluestein, 2012: The Second Verification of the Origins of Rotation in Tornadoes Experiment: VORTEX2. *Bull. Amer. Meteor. Soc.,* **93,** 1147–1170.

Yussouf, N., and D. J. Stensrud, 2012: Comparison of single-parameter and multiparameter ensembles for assimilation of radar observations using the ensemble Kalman filter. *Mon. Wea. Rev.,* **140,** 562–586.

Zhang, F., C. Snyder, and J. Sun, 2004: Impacts of initial estimate and observation availability on convective-scale data assimilation with an ensemble Kalman filter. *Mon. Wea. Rev.,* **132,** 1238–1253.